

UKAEA-CCFE-PR(25)359

Edoardo Tomasina 1, 2 M.J.Markl 3 L.Pigatto 2  
D.Ryan 4 A.Kirk 4 C.G.Albert 3 E.Viezzer 5 Y.Q. Liu 6  
T. Bolzonella 2 MAST-U team EUROfusion Tokamak

Exploitation Team 1 Universit`a degli Studi di  
Padova, Padova, Italy. 2 Consorzio RFX (CNR,

ENEA, INFN, Universit`a di Padova, Acciaierie  
Venete SpA), Corso Stati Uniti 4, 35127, Padova

(Italy). 3 Fusion@OFAW, Graz University of  
Technology, Graz, Austria. 4 UKAEA, Culham

Campus Abingdon, UK. 5 D. Ruiz Pastor

Atomic, Molecular, Nuclear Physics, University of  
Seville, Seville, Spain. 6 General Atomics, PO Box

85608, San Diego, CA 92186-5608, USA.

# Linear and quasi-linear modeling in view of ELM control in MAST-U: effects of Error Fields and pedestal characteristics

Enquiries about copyright and reproduction should in the first instance be addressed to the UKAEA Publications Officer, Culham Science Centre, Building K1/O/83 Abingdon, Oxfordshire, OX14 3DB, UK. The United Kingdom Atomic Energy Authority is the copyright holder.

The contents of this document and all other UKAEA Preprints, Reports and Conference Papers are available to view online free at [scientific-publications.ukaea.uk/](https://scientific-publications.ukaea.uk/)

# Linear and quasi-linear modeling in view of ELM control in MAST-U: effects of Error Fields and pedestal characteristics

Edoardo Tomasina 1, 2 M.J.Markl 3 L.Pigatto 2 D.Ryan 4 A.Kirk 4 C.G.Albert 3 E.Viezzer 5 Y.Q. Liu 6 T. Bolzonella 2 MAST-U team EUROfusion Tokamak Exploitation Team 1 Universit`a degli Studi di Padova, Padova, Italy. 2 Consorzio RFX (CNR, ENEA, INFN, Universit`a di Padova, Acciaierie Venete SpA), Corso Stati Uniti 4, 35127, Padova (Italy). 3 Fusion@OEAW, Graz University of Technology, Graz, Austria. 4 UKAEA, Culham Campus, Abingdon OX14 3DB, UK. 5 Department of Atomic, Molecular, Nuclear Physics, University of Seville, Seville, Spain. 6 General Atomics, PO Box 85608, San Diego, CA 92186-5608, USA.



# Linear and quasi-linear modeling in view of ELM control in MAST-U: effects of Error Fields and pedestal characteristics

E.Tomasina<sup>1,2</sup>, M.J.Markl<sup>3</sup>, L.Pigatto<sup>2</sup>, D.Ryan<sup>4</sup>, A.Kirk<sup>4</sup>,  
C.G.Albert<sup>3</sup>, E.Viezza<sup>5</sup>, Y.Q. Liu<sup>6</sup>, T. Bolzonella<sup>2</sup>, MAST-U  
team\* and the EUROfusion Tokamak Exploitation Team\*\*

<sup>1</sup>Università degli Studi di Padova, Padova, Italy. <sup>2</sup>Consorzio RFX (CNR, ENEA, INFN, Università di Padova, Acciaierie Venete SpA), Corso Stati Uniti 4, 35127, Padova (Italy). <sup>3</sup>Fusion@OEAW, Graz University of Technology, Graz, Austria.

<sup>4</sup>UKAEA, Culham Campus, Abingdon OX14 3DB, UK. <sup>5</sup> <sup>6</sup> Department of Atomic, Molecular and Nuclear Physics, University of Seville, Seville, Spain. <sup>6</sup>General Atomics, PO Box 85608, San Diego, CA 92186-5608, USA. \*See the author list of J. Harrison et al 2019 Nucl. Fusion 59 112011. \*\*See the author list of E. Joffrin et al 2024 Nucl. Fusion 64 112019

E-mail: edoardo.tomasina@igi.cnr.it

**Abstract.** Edge Localized Modes (ELMs) pose a critical challenge to the safety and performance of plasma-facing components in tokamaks due to their periodic expulsion of heat and particles. This study investigates the behavior of various figures of merit for evaluating Resonant Magnetic Perturbations (RMPs) as a tool for achieving ELM control in the spherical tokamak MAST-U. A combination of linear and quasi-linear modeling workflows, including MARS-F (single-fluid resistive MHD) and KilCA (two-fluid kinetic) codes, was used to analyze plasma responses to RMPs under realistic operational conditions. To address recent experimental results, a detailed model for the  $n = 2$  intrinsic Error Field (EF) generated by the Poloidal Field (PF) coil system was developed, and the plasma response to this EF was computed. Results indicate that the  $n = 2$  EF is, at least, of the same order of magnitude of the perturbations introduced by the external RMP coils. In particular, the EF was found to significantly shift the optimal points of the analyzed metrics, affecting the effectiveness of ELM mitigation strategies. The study further explores the dependence of ELM control on kinetic parameters through a systematic scan of the pedestal density profile. Findings reveal that different metrics exhibit varying degrees of robustness to changes in the density gradient. While radial field-based and torque-based metrics optima are found to be more solid, displacement-based metrics are more sensitive to variations, emphasizing the importance of accurate equilibrium reconstruction and robust kinetic modeling. These results underscore the critical need for addressing intrinsic EF correction and integrating kinetic considerations when designing ELM control strategies.

## 1 Introduction

Edge Localized Modes (ELMs) are pressure-current hybrid MHD instabilities that periodically lead to the violent expulsion of heat and particles in a filamentary fashion when plasmas in tokamak configurations reach the so-called H-mode confinement [1]. In reactor-scale experiments such as ITER, controlling ELMs is crucial to ensure the safety of plasma-facing components, as the power deposited by ELM bursts scales with the size of the device [2]. Various techniques have been explored for ELM control, which can be broadly categorized into pacing, mitigation, and suppression strategies. ELM pacing is typically achieved through pellet injection [3], whereas mitigation and suppression are generally realized via the application of Resonant Magnetic Perturbations (RMPs) through external, non-axisymmetric coils [4]. Mitigation refers to reducing the amplitude while increasing the frequency of ELM events [5, 6], whereas suppression describes a regime in which ELMs are completely eliminated [7].

Notably, ELM suppression has never been observed in tight aspect ratio, or spherical, tokamaks [8]. While ELM mitigation via RMPs was demonstrated in the earlier MAST experiment [9], replicating this success in MAST-U has proven challenging. Recent MAST-U campaigns have yielded mixed results, ranging from significant effects leading to mode-locking and disruptions to negligible impact [10]. Key differences between MAST-U and its predecessor include an increase in the maximum plasma current amplitude, accompanied by a reduction in the number of independently powered non-axisymmetric coils [11]. This reduction was necessary to accommodate the installation of the off-axis Neutral Beam Injector (NBI) and several diagnostics views. However, as a consequence, it also constrained the achievable toroidal spectrum. Nevertheless, considering the increased plasma size in MAST-U which effectively brings the plasma boundary closer to the coils, similar magnitudes of the perturbed fields are achieved [10]. Detailed specifications of the RMP coil system in MAST-U are provided in [10]. Moreover, so far RMP experiments have been conducted only in Connected Double Null (CDN) discharges as no Single Null (SN) scenario was yet available. It is known that ELM control in CDN discharges is more challenging due to the reduced plasma response on the High Field Side (HFS) [12]. Since previous MAST experiments, modeling and empirical evidences have suggested the presence of a residual Error Field (EF) dominated by a  $n = 2$  component (with  $n$  being the discrete number denoting toroidal periodicity)[10]. While in previous ELM control experiments the  $n = 2$  was less impacting because of the access to higher toroidal perturbations (see for ex: [5]), in the current state of the operations the EF could have a non-negligible impact. This could, in principle, explain the discrepancies between experimental results and predictions of the optimal phase alignment for achieving mitigation when operating with the RMP coils in  $n = 2$  configuration.

Expanding the modeling effort to understand these discrepancies, this work investigates the plasma response to external magnetic perturbations in MAST-U. The study evaluates and compares the roles of different metrics, both fluid and kinetic, while assessing the influence of kinetic parameters. Specifically, the magneto-hydrodynamic, resistive, linear code MARS-F [13] is applied to compute the perturbation field resulting from the combined effects of RMP coil currents and the plasma response. Classical fluid metrics

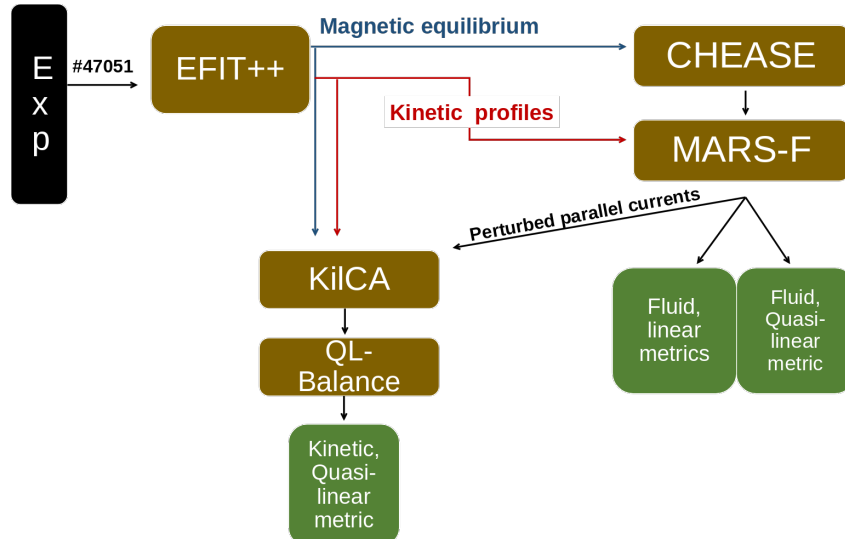


Figure 1: Summary of the complete modeling pipeline.

derived from linear and quasi-linear response theories, are analyzed and re-evaluated by incorporating an EF model. Additionally, a quasi-linear figure of merit based on a kinetic plasma response model, computed within the KilCA framework [14] and previously applied to AUG results, is integrated into the analysis.

The kinetic parameters are crucial in addressing plasma response challenges. Investigating these requires robust diagnostics, diverse modeling tools, and dedicated experiments. In this study, the impact of variations in the edge density profile has been numerically examined, motivated by the recent installation of a cryopump in the MAST-U lower divertor, expected to operate in current and future campaigns. The behavior of the various metrics is analyzed and compared as the electron density profile in the pedestal region is systematically scanned.

In the following: the numerical models used throughout the work are presented in Section 2, the different figures of merit applied are discussed in Section 3, whereas the separatrix density scan is reported in Section 4. In Section 5 the EF model is presented and its implications are briefly discussed. Finally, Section 6 includes the conclusions and the work summary.

## 2 Modeling workflow

In this work, starting from the experimental discharges, a combination of numerical workflows has been implemented with the scope of deriving and compare metrics for the optimization of RMPs in terms of ELM control. The summary of the complete process is summarized in Fig.1. Results are mainly based on the application of the CHEASE/MARS-F workflow, where CHEASE is a well-established Grad-Shafranov solver [15] used to generate equilibrium inputs for subsequent plasma response calculations. The starting point for any plasma response evaluation is the equilibrium configuration, to which a perturbation can then be applied. To maintain consistency with experimental observations, the reconstructed equilibrium of an ELMy discharge from the MU-02 campaign has been chosen, specifically discharge #47051. A closely related

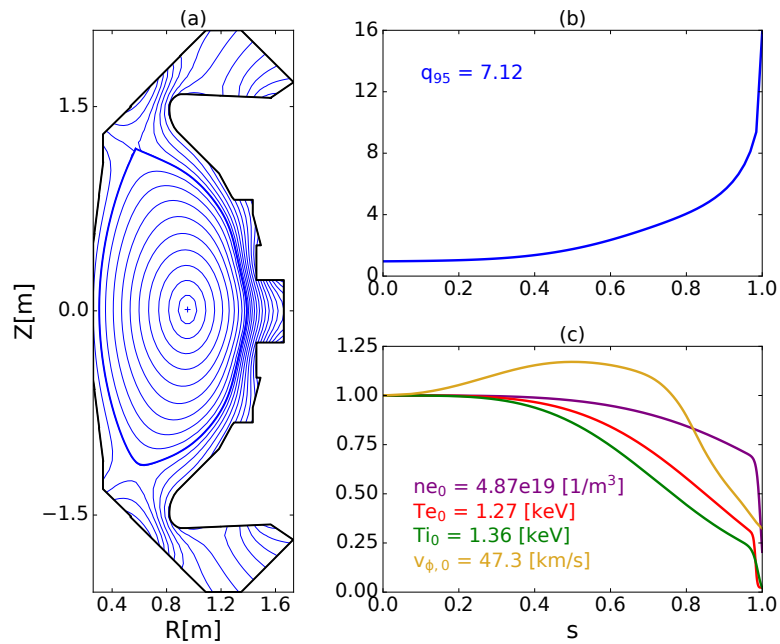


Figure 2: Equilibrium. *Left*: Magnetic flux reconstruction at 611 ms. *Right, top*: MSE constrained safety factor profile. *Right, bottom*: Kinetic profiles (EFIT++ reconstructed) provided as MARS-F inputs.

discharge, #47052, was previously modeled with MARS-F to determine the optimal coil phasing for ELM control experiments in the MU-03 campaign [10]. The equilibrium is prepared by running CHEASE on magnetically constrained data that has been processed with the EFIT++ [16] code. In MAST-U, equilibrium reconstructions are typically constrained using Motional Stark Effect (MSE) measurements [17], which provide a physical constraint on the internal current profile and thus on the safety factor ( $q$ ) profile. Furthermore, to closely replicate experimental conditions, kinetic radial profiles are fitted within separate EFIT++ runs and provided to MARS-F as additional inputs. MAST-U diagnostics can reliably measure electron temperature and density, ion temperature and toroidal rotation velocity, though the latter two are only available when the diagnostic NBI is active. Since MARS-F cannot explicitly handle the X-point singularity at the plasma boundary, a smoothing routine is applied in CHEASE before preparing inputs for plasma response computations. This smoothing reduces the edge safety factor ( $q_a$ ) value but does not affect  $q_{95}$ . Previous studies have shown that that this kind of variations in  $q_a$  still yield similar plasma response spectra [18]. Fig.2 presents the equilibrium and kinetic profiles used for the MARS-F computations. It is important to note that, at this level, the kinetic profiles do not influence the equilibrium computation performed with CHEASE; the implications of this will be discussed in a subsequent section.

MARS-F solves the linearized MHD equations under the single-fluid, resistive approximation, within the resistive-inertial regime. These MHD equations account for a generic toroidal flow and couple with RMP source terms, modeled as an antenna problem. The system is expressed as follows:

$$i(\Omega_{RMP} + n\Omega)\boldsymbol{\xi} = \mathbf{v} + (\boldsymbol{\xi} \cdot \nabla\Omega)R\hat{\phi} \quad (1)$$

$$\begin{aligned} i(\Omega_{RMP} + n\Omega)\mathbf{v} &= -\nabla P + \mathbf{j} \times \mathbf{B} + \mathbf{J} \times \mathbf{b} \\ &\quad - \rho[2\Omega\hat{Z} \times \mathbf{v} + (\mathbf{v} \cdot \nabla)R\hat{\phi}] \\ &\quad - \rho k_{//} |\kappa_{//} v_{th,i}| (\mathbf{v} + (\boldsymbol{\xi} \cdot \nabla V_0))_{//} \end{aligned} \quad (2)$$

$$i(\Omega_{RMP} + n\Omega)\mathbf{b} = \nabla \times (\mathbf{v} + \mathbf{B}) + (\mathbf{b} \cdot \nabla\Omega)R\hat{\phi} - \nabla \times (\eta\mathbf{j}) \quad (3)$$

$$i(\Omega_{RMP} + n\Omega)\mathbf{p} = -\mathbf{v} \cdot \nabla P - \Gamma P \nabla \cdot \mathbf{v} \quad (4)$$

+

$$\mathbf{j} = \nabla \times \mathbf{b}, \nabla \times \mathbf{b} = \mathbf{j}_{RMP}, \nabla \cdot \mathbf{j}_{RMP} = 0 \quad (5)$$

In this formulation, bold quantities represent 3D vectors, uppercase variables denote equilibrium quantities, and lowercase variables indicate perturbed quantities. The unit vector  $\hat{\phi}$  points in the toroidal direction, while  $\hat{Z}$  indicates the vertical direction in the poloidal plane. For physical quantities,  $\mathbf{J}$  represents the electric current,  $\mathbf{B}$  the magnetic field,  $\boldsymbol{\xi}$  the perturbed displacement,  $\mathbf{v}$  the perturbed velocity,  $\mathbf{P}$  the pressure,  $\rho$  the plasma density, and  $\eta$  the resistivity. Additionally,  $R$  is the plasma major radius,  $\Omega$  is the toroidal rotation frequency, and  $V_0 = R\Omega\hat{\phi}$ . The toroidal mode number is denoted as  $n$ , and  $\Gamma$  is the adiabatic index. The parallel wave number,  $\kappa_{//} = (n - \frac{m}{q})$  is defined using the poloidal mode number ( $m$ ) and the safety factor  $q$ . Here,  $v_{th,i}$  represents the thermal ion velocity, and  $k_{//}$  is a numerical coefficient that mimics parallel sound damping [19]. In this study, a strong damping regime is assumed, corresponding to  $k_{//} = 1.5$ . The input RMP current,  $\mathbf{j}_{RMP}$  is modeled as sinusoidal along the toroidal angle, with periodicity  $n$ , such that  $\mathbf{j}_{RMP} \propto e^{in\phi}$ . Details of the implementation of the active coil currents in the code can be found in Appendix A of [20].

### 2.1 *KilCA/QL-Balance kinetic model*

External perturbation are usually effective in controlling ELMs only when they successfully penetrate into the plasma. As an initial response to external RMPs, parallel currents are built-up in correspondence to the relative resonant surfaces. These currents are oriented to produce a radial field opposite to the externally induced one in the attempt to reduce the perturbation, hence they are also referred to as *shielding currents*. The shielding to the external perturbation is proportional to the plasma flow. In principle, the parallel currents will interact with the radial field causing an electromagnetic torque which onsets a feedback loop that eventually may lead to the flow braking and to the loss of shielding. The non-linear process for which the plasma response eventually fails in producing shielding is known as *bifurcation* [21]. Due to this cyclic nature of the RMPs dynamic, a quasi-linear model requires to be employed when studying penetration. In particular, within the fluid framework perturbation penetration is assumed to be related to the bulk fluid braking exerted by the induced external fields. Alternatively, when considering the kinetic framework, the penetration is associated to the electron fluid braking.

Here, a quasi-linear kinetic response model has been applied to study penetration effectiveness with the KilCA/QL-Balance workflow. KilCA is a linear kinetic Maxwell equation solver in cylindrical geometry based on a finite Larmor radius expansion [14]. The equations that are solved in cylinder coordinates  $(r, \vartheta, z)$  are

$$\nabla \times \mathbf{E} - \frac{i\omega}{c} \mathbf{B} = 0, \quad \nabla \times \mathbf{B} + \frac{i\omega}{c} \mathbf{E} = \frac{4\pi}{c} (\mathbf{j} + \mathbf{j}_{\text{RMP}}). \quad (6)$$

Note the time-harmonic dependency and the use of CGS units. Also, due to the periodicity of the cylindrical model, a Fourier expansion in toroidal and poloidal angle can be employed. This casts the problem into a set of ordinary differential equations in the radial variable  $r$ . To connect the model to experimental profiles, the radial variable is set equal to an effective radius  $r \equiv r_{\text{eff}} = \sqrt{2\psi_{\text{tor}}/B_{\text{ref}}}$ , where  $\psi_{\text{tor}}$  is the toroidal flux and  $B_{\text{ref}}$  is the reference magnetic field of the equilibrium at the magnetic axis. The experimental profiles given as a function of the square root of the normalized poloidal flux are mapped to  $r_{\text{eff}}$ .

The current density in Ampere's law in (6) is given by two parts: the RMP current density provided by an antenna (i.e. the active coil) outside the plasma  $\mathbf{j}_{\text{RMP}}$  and the plasma response current  $\mathbf{j}$ . The plasma response current is determined in kinetic theory with a finite Larmor radius expansion to order  $N_{\text{FLR}}$  as

$$j_{mn}^i(r) = \frac{1}{r} \sum_{k,k'=0}^{N_{\text{FLR}}} (-1)^k \frac{\partial^k}{\partial r^k} \left( r \sigma_{kk',mn}^{il}(r) \frac{\partial^{k'}}{\partial r^{k'}} E_{mnl}(r) \right). \quad (7)$$

Where the apex  $i$  identifies the spatial components and the species index is suppressed here for brevity. The current is determined for a specific poloidal and toroidal mode number  $m$  and  $n$ , respectively, by the conductivity tensor  $\sigma$ . The conductivity tensor is derived from the solution to the kinetic equation with a Fokker-Planck type collision operator in the Ornstein-Uhlenbeck approximation including an energy-preserving integral term. For more details see [14, 22]. In the following,  $N_{\text{FLR}} = 1$  is used.

QL-Balance [14] is a quasi-linear 1D radial transport code which takes inputs from the linear kinetic response. This model solves transport equations for the electron density, electron and ion temperature, and the toroidal rotation velocity based on drift-kinetic transport coefficients  $D^{\text{ql}}$  that are determined by the electromagnetic field perturbations of KilCA. Anomalous transport is taken into account here by a diffusion coefficient  $D^{\text{a}}$ , which is set to a constant value  $D^{\text{a}} = 1 \text{ m}^2/\text{s}$ . Additionally, to determine the radial electric field via the ion force balance, the poloidal rotation is calculated by the drift-kinetic solver NEO-2 [23, 14].

*2.1.1 Toroidal rescaling* A drawback of the cylinder model is the lack of poloidal mode coupling which can significantly affect the magnitude of the shielding [24]. This issue was addressed already for the modeling of ASDEX-Upgrade in [14] by rescaling the electromagnetic fields calculated by KilCA with a scaling factor

$$C_{mn} = \frac{I_{\parallel,mn}^{\text{tMHD}}}{I_{\parallel,mn}^{\text{KilCA}}}, \quad (8)$$

given by the integrated parallel shielding currents determined by a chosen toroidal MHD code ( $I_{\parallel, mn}^{\text{MHD}}$ ) and by KilCA ( $I_{\parallel, mn}^{\text{KilCA}}$ ). In previous work studying ASDEX-Upgrade, the toroidal ideal MHD code GPEC [25][26] was used. Here, the toroidal shielding current is provided by MARS-F. The computation of the parallel current in MARS-F and its integration into the KilCA current are summarized in [Appendix A](#), the latter part is also exhaustively described in [14]. The rescaling is motivated by the similarities between the plasma response in the fluid and kinetic models in the case of strong shielding. For more details, see Ref.[14].

### 3 Metrics

When preparing an ELM control experiment, the routine procedure involves running a linear MHD code, such as GPEC [27] or MARS-F, to quickly predict the coil phasing that optimizes a specific objective function or metric. In MAST and ASDEX [6], successful experiments have been conducted by maximizing the magnitude of the radial component of the edge-resonant perturbation field,  $b_{edge, res}^1$ , which is nominally defined as:  $\frac{\mathbf{b} \cdot \nabla \psi}{\mathbf{B}_0 \cdot \nabla \phi} \frac{q}{R_0^2 B_0}$  with the subscript 'edge, res' identifying the Fourier harmonic which resonate at the last pitch-aligned surface (i.e  $m = n \cdot q_{edge}$ ). Here  $\psi$  and  $\phi$  are respectively the poloidal and toroidal fluxes,  $R_0$  is the machine axis position and  $B_0$  is the equilibrium magnetic field at the axis. This quantity is calculated in straight field line (SFL) coordinates, or PEST-like, within MARS-F and serves as a figure of merit for quantifying the perturbation effectively injected into the edge plasma, accounting for the plasma response. This metric is particularly valuable for coil systems that may struggle to surpass the threshold field or input current required to achieve ELM mitigation. It is especially useful for higher  $n$  perturbations, which tend to penetrate less effectively due to the higher number of rational surfaces concentrated in the edge and to a faster spatial decay. At lower  $n$  and for sufficiently powerful coil systems, the injected perturbation may trigger a locked mode [21], potentially leading to plasma termination. In such cases, a figure of merit that decouples the effects of the perturbation at the edge and core is preferred. The objective is to degrade the edge confinement just enough to stabilize the ELM while preserving favorable conditions in the plasma core [28]. To this end, metrics such as  $\xi_X^N / \xi_{mid}^N$  or  $\tau_{edge} / \tau_{core}$  are often maximized. The first metric,  $\xi_X^N / \xi_{mid}^N$ , represents the ratio of the normalized plasma displacement at the X-point to that at the mid-plane. This is considered a robust marker of confinement degradation induced by the application of RMPs. Studies have shown that the X-point displacement tends to couple strongly with a peeling-like plasma response, which is closely associated with edge stability, whereas mid-plane displacement is typically linked to a kink-like response that penetrates further into the plasma core [29]. This behavior has been corroborated by ELM mitigation experiments conducted in ASDEX and MAST [6]. Notice that, since in MARS-F the X-points are not reproduced, the  $\xi_X^N$  displacements are computed by averaging the regions around the upper most and lower most points of the boundary. The second metric,  $\tau_{edge} / \tau_{core}$  corresponds to the ratio of the integrated total torque injected, by the RMPs, into the edge region to that injected in the core region. This metric provides a complementary view for evaluating the effects of RMPs on edge and core dynamics.

*Linear metrics*

MARS-F operates within the linear physics framework, meaning that the superposition of computed solutions also constitutes valid solutions. Mathematically, if  $X$  is a generic solution, the expression  $X_{tot} = A \cdot X_L + B \cdot X_U e^{i\Delta\phi}$  remains a solution in MARS-F. Here,  $A$  and  $B$  are arbitrary coefficients, and  $\Delta\phi$  represents the relative toroidal variation between the coil rows. In MAST-U, two rows of ELM coils are currently available. The coils are placed in-vessel on the Low Field Side (LFS), covering the whole toroidal angle. The two rows have different number of coils with the Upper row having 4 coils and the Lower having 8, hence yielding less space between each of them. In this work the relative phase between respective coils at the same toroidal position is defined as  $\phi_{LOWER} - \phi_{UPPER}$ , that is: the upper coil row is treated as fixed at  $\phi_{UPPER} = 0^\circ$ , while the lower coil row, which has a greater number of degrees of freedom, is varied. This property enables a rapid exploration of all possible coil-set combinations in terms of input current amplitude and toroidal phasing. Such efficiency is leveraged to identify optimal configurations for addressing the ELM mitigation or suppression problem by analyzing the behavior of various (linear) output quantities while scanning the parameter space of the input currents. The optimization results for the first two metrics are illustrated in Fig. 3 for the two toroidal mode numbers,  $n = 1$  and  $n = 2$ . The computed optimal phasing values for each metric align well with those reported in [10]. As anticipated, the optimal phase is sensitive to the applied toroidal mode number but exhibits similar trends in both cases. Notably, the plasma response always introduces a shift of the optimal phase, of  $\sim 90^\circ$  for the  $n = 1$  and  $\sim 40^\circ$  for the  $n = 2$ . Additionally, the displacement metric achieves optimization at nearly the same relative phase when considering the displacement at both the lower and upper X-points. Strictly in terms of magnitudes, the displacement at the upper X-point exceeds that at the lower X-point for both the  $n = 1$  and  $n = 2$  cases, measuring  $\xi_U = 0.49\text{mm/kAt}$ ,  $\xi_L = 0.3\text{mm/kAt}$  and  $\xi_U = 0.39\text{mm/kAt}$ ,  $\xi_L = 0.18\text{mm/kAt}$  respectively.

*Quasi-linear fluid metric*

The torque induced by externally generated 3D fields is inherently a non-linear effect, as it depends quadratically on the perturbation. In MARS-F, various types of physical torques can be calculated based on the plasma response results. Specifically, the electromagnetic ( $\mathbf{j} \times \mathbf{b}$ ), Neoclassical Toroidal Viscosity (NTV), and Reynolds stress (REY) torque sources are included in this work. The  $\mathbf{j} \times \mathbf{b}$  and REY torques are purely MHD-driven, with the former originated by the interaction between the perturbed field ( $b^1$ ) and the shielding currents built in response to it ( $j^2$ ) and the latter associated to the Reynolds stress tensor term, that is  $\propto (\mathbf{v} \cdot \nabla)\mathbf{v}$ . A comprehensive evaluation of the NTV torque, instead, would require a full kinetic or drift-kinetic treatment. However, in MARS-F, an analytic formula is implemented to bridge different collisionality regimes, as detailed in [30] and [31]. Comparisons of this NTV computation with kinetic treatments have demonstrated qualitative agreement [32]. To leverage the linearity advantages of the framework, some manipulation of the torque outputs is necessary. For this purpose, a semi-analytic algorithm is integrated into the code to construct a torque matrix that

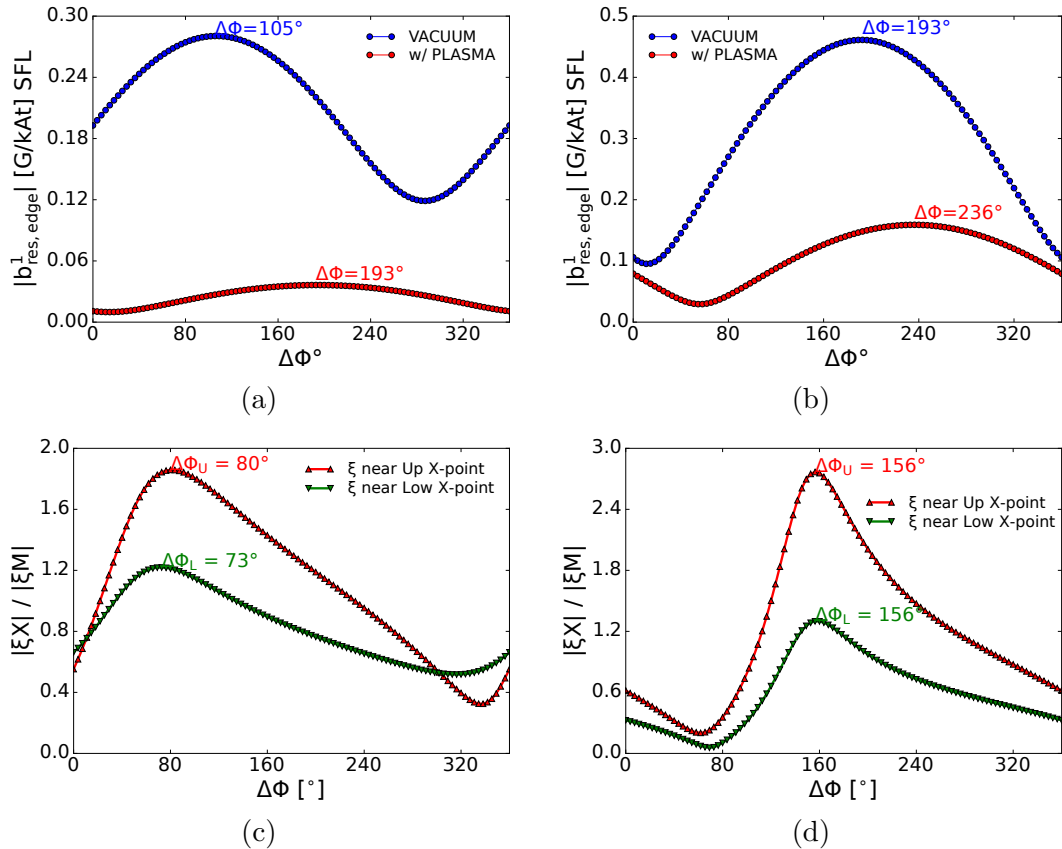


Figure 3: Fluid linear metrics dependence on relative coil phase  $\Delta\phi$ . *a,c*:  $n=1$ , *b,d*:  $n=2$ . *a,b*:  $|b^1_{edge,res}|$  metric, with **blue**: vacuum only and **red**: vacuum + plasma response. *c,d*:  $\xi_{X-point}^N / \xi_{mid-plane}^N$  metric, with **red**:  $\xi_{upperX-point}^N$  and **green**:  $\xi_{lowerX-point}^N$

incorporates terms accounting for mutual coupling between the rows of coils [33]. This approach generalizes the torque computation for arbitrary input current values  $\mathbf{I}$ , as described by the following relationship:

$$\Pi^\alpha(s) = \mathbf{I} \cdot \Pi_M^\alpha(s) \cdot \mathbf{I}^* = [I_U \quad I_L] \begin{bmatrix} \Pi_{UU}^\alpha & \Pi_{UL}^\alpha \\ \Pi_{LU}^\alpha & \Pi_{LL}^\alpha \end{bmatrix} (s) \begin{bmatrix} I_U^* \\ I_L^* \end{bmatrix} \quad (9)$$

Where  $\Pi^\alpha(s)$  is the surface-averaged torque density, with  $s = \sqrt{\frac{\psi - \psi_{axis}}{\psi_{edge} - \psi_{axis}}}$  being the MARS-F radial coordinate and  $\alpha = \mathbf{j} \times \mathbf{b}, NTV, REY$ . The superscript  $*$  denotes the complex-conjugate of the vector.

In order to maximize the  $\tau_{edge}/\tau_{core}$  ratio, we first define  $\Pi^{tot} \equiv \sum_\alpha \Pi^\alpha$  and then take the radial integral separating the core and edge regions:

$$\tau_{core} \equiv \int_0^{0.89} \Pi^{tot}(s) ds \quad (10)$$

$$\tau_{edge} \equiv \int_{0.89}^1 \Pi^{tot}(s) ds \quad (11)$$

Where the boundary among the two regions has been set  $s = 0.89$ . Of course the separation between the two regions retains a degree of freedom, however, as long as the edge region contains the pedestal, the results are fairly robust to variation of this

parameter[34]. In Fig.4, a scan in input current for determining the total integrated torque is reported for both toroidal mode numbers  $n = 1$  and  $n = 2$  and for both the edge and the core regions. In the scan the upper row of coils is again considered fixed while the lower row is allowed to vary between  $[0 - 360]^\circ$ . For both rows the input current is also scanned in amplitude, ranging between  $[1 - 8]$ kAt. Notice that the maximum current achievable in MAST-U active coils consists of a total of 8kAt. The result of the torque ratio optimization is shown in Fig.5. Notably, this metric appears to be strongly robust against the toroidal mode number variation. In particular, the torque ratio seems to be always optimized when the relative phase between the two rows of coils corresponds to  $180^\circ$ . This should be due to the strong decoupling between edge and core torques. While this decoupling is predominant in the  $n = 2$  configuration, for the  $n = 1$  the optimal phase follows the request of maximizing the edge total torque, whereas the core appears to be less impacted by the phase variation.

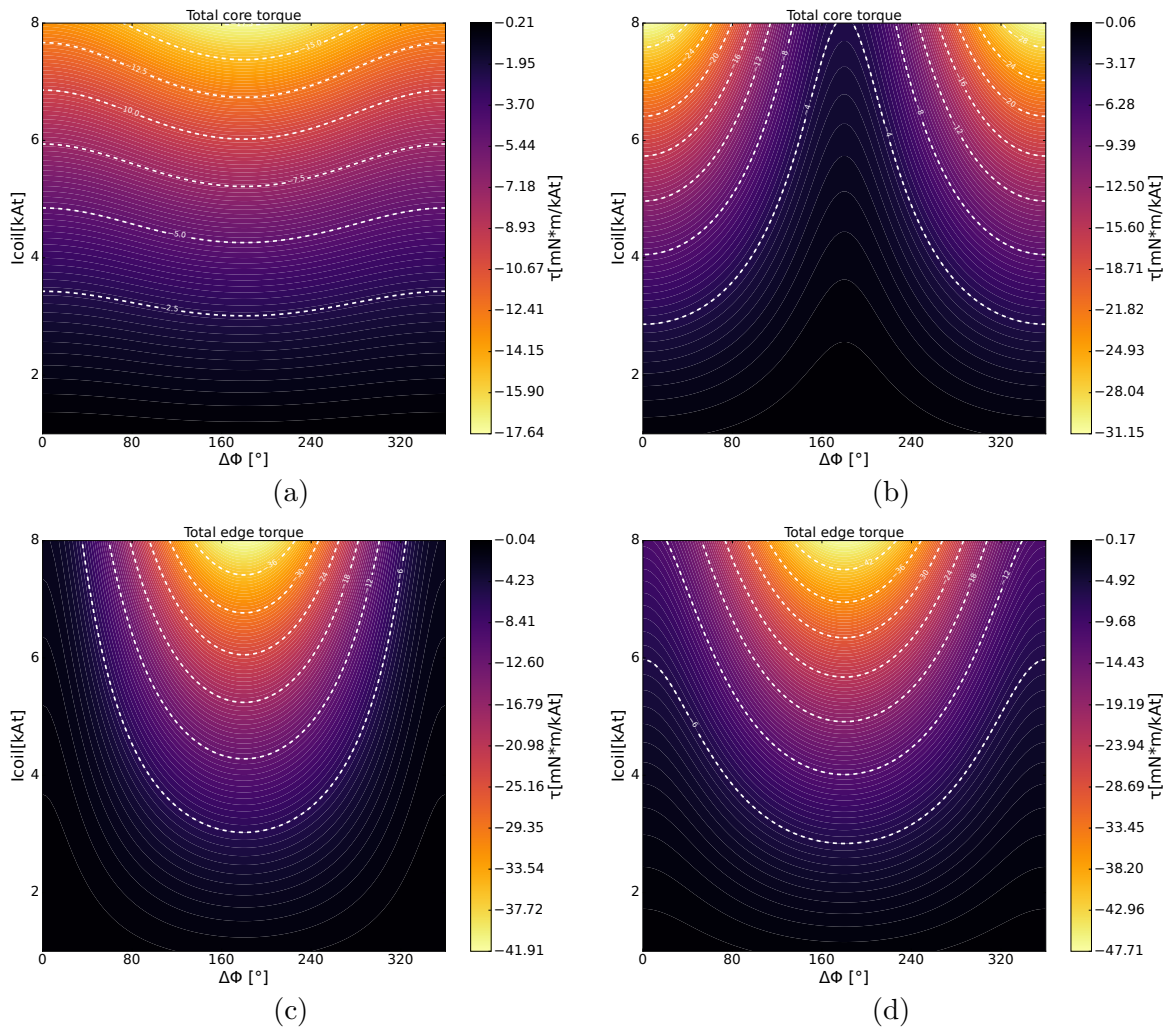
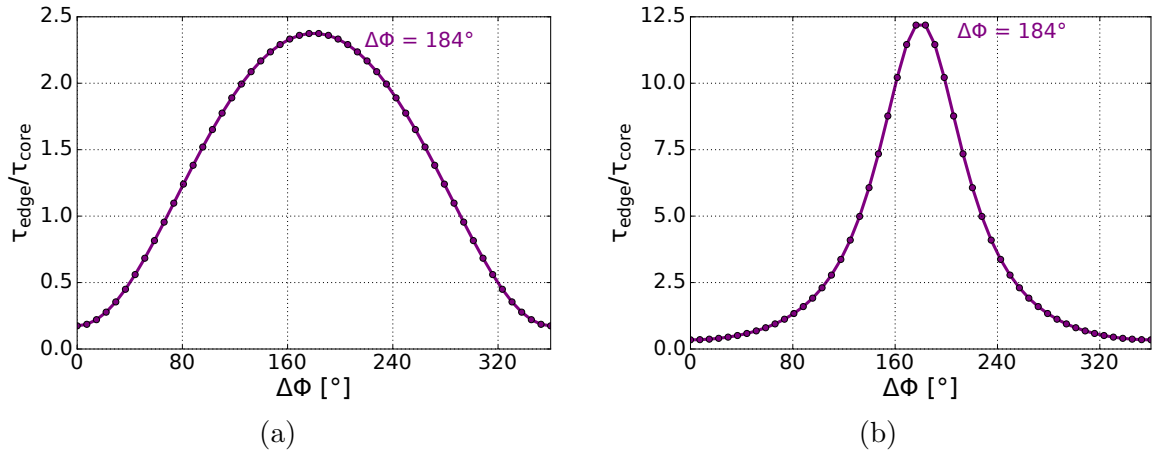
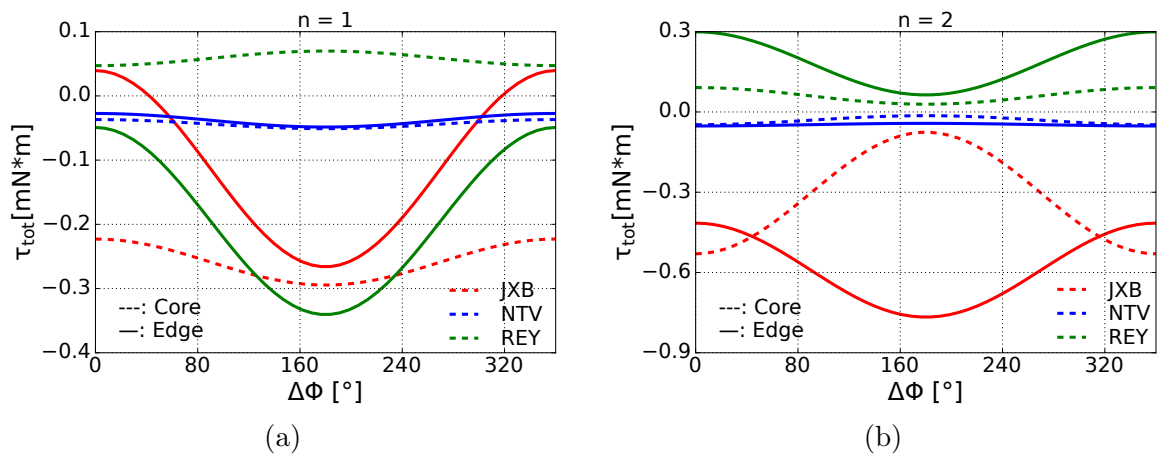


Figure 4: Integrated total torque obtained by varying the current magnitude and relative phase between the upper and lower coilsets. *a*:  $n = 1$ , core region, *b*:  $n = 2$ , core region. *c*:  $n = 1$ , edge region. *d*:  $n = 2$ , edge region

In order to better understand this behavior, we can analyze more in detail each source of torque, in each spatial region, at the variation of  $\Delta\Phi$ . This is shown in Fig.6 for both the  $n = 1$  and the  $n = 2$  mode numbers.


 Figure 5:  $\tau_{edge}/\tau_{core}$  vs  $\Delta\phi$  for  $n = 1$  (a) and  $n = 2$  (b) configurations.

 Figure 6: Integral torques split by source and region. *a*:  $n = 1$ , *b*:  $n = 2$ . Solid lines corresponds to the edge while dashed lines identify the core. A color code is used to distinct each torque source, so red:  $\mathbf{j} \times \mathbf{b}$ , blue: NTV and green: REY

Focusing first on the  $n = 1$  component, within the core region (dashed line in the figure) it appears that the REY and  $\mathbf{j} \times \mathbf{b}$  torques are in competition, with the latter being bigger hence driving the global flow braking. Moving in the edge region the picture changes, for most of the  $\Delta\Phi$  values  $\mathbf{j} \times \mathbf{b}$  and REY torques are aligned in braking the flow. The optimum of the torque ratio metric is justified observing that the integral torque in the core region, of each source, is only slightly changing while varying the coils relative phase, whereas in the edge, the braking is strongly amplified at  $\Delta\Phi \sim 180^\circ$ , hence satisfying the requirement. Notably, depending on the phase, both  $\mathbf{j} \times \mathbf{b}$  and REY torque components can individually be oriented toward plasma acceleration, however when summing them together, the global torque appears to be always in the counter-flow direction.

For the  $n = 2$  case the picture is somehow different, even if leading to the same conclusions: now REY and  $\mathbf{j} \times \mathbf{b}$  are always in competition with the viscous term trying to compensate the electromagnetic-induced braking. However the  $\mathbf{j} \times \mathbf{b}$  is always leading the global behavior. The core torque now is always smaller than the edge one, in particular, the  $\mathbf{j} \times \mathbf{b}$  is minimal in the exact correspondence of the correspondent edge maximum, which is located, as expected, at  $\Delta\Phi \sim 180^\circ$ , this allows to achieve simultaneously both

the edge and core torque requirements. Moreover, as the relative phase is increased, the positive edge REY torque and the negative core  $\mathbf{j} \times \mathbf{b}$  both decrease while the negative edge  $\mathbf{j} \times \mathbf{b}$  increases in magnitude. This allows to simultaneously satisfy both the edge torque maximization/core torque minimization requirements. Finally, the NTV contribution to the total toroidal torque is always at least one order of magnitude less than the others. Therefore evolution of the velocity profile can be interpreted as being predominantly driven by the competition between the electromagnetic braking (induced by the external coils) and the correspondent inertial viscous drag of the plasma.

### Quasi-linear kinetic metric

To determine the actual effectiveness of the perturbations achieved with the MAST-U ELM coil system, the KilCA/QL-Balance quasi-linear framework has been implemented. Within the framework a criterion for the bifurcation of an arbitrary mode was defined in [14]. This criterion is characterized by a ratio of diffusion coefficients,

$$D_{mn} \equiv \left. \frac{D_{e,22}^{\text{ql}}}{D^{\text{a}}} \right|_{r=r_{mn}} \geq 1. \quad (12)$$

Here,  $D_{e,22}^{\text{ql}}$  is the quasi-linear electron heat diffusion coefficient determined within drift-kinetic theory employing a Fokker-Planck collision operator in the Ornstein-Uhlenbeck approximation. For the expression of the quasi-linear diffusion coefficient see Ref. [14].  $D^{\text{a}}$  is the anomalous diffusion coefficient, which is set to 1 m<sup>2</sup>/s. The criterion is based on the observation that a feedback loop enabling bifurcation, by local rotation braking or acceleration to approach the electron fluid resonance, is triggered when the quasi-linear diffusion increases to the size of the anomalous one. The diffusion ratio is evaluated at the effective radius  $r_{mn}$  of the resonant surface. Since mode penetration of a resonant surface on the pedestal top is commonly assumed to be a requirement for ELM suppression [35], the focus of this metric are modes located near the pedestal top.

In this work, the criterion (12) as a metric for ELM control is applied. In particular, when scanning over the differential phase  $\Delta\Phi$ , the maximum of  $D_{mn}$  indicates the optimal coil configuration for mode penetration while the value assumed by the ratio suggests its actual effectiveness.

A first qualitative assessment can be provided by the analytic expression of the quasi-linear diffusion coefficient in constant- $\psi$  approximation given by equation (51) in [14]. The expression shows that the coefficient is proportional to the parallel shielding current squared,  $D_{e,22}^{\text{ql}} \propto |I_{\parallel}|^2$ . This statement is independent on the model in which the current is calculated. Hence, since the  $\Delta\Phi$  toroidal dependence can only be introduced from MARS-F results, assuming constant anomalous diffusion, the optimum of the kinetic metric  $D_{mn}$  has to coincide with the maximum of the shielding currents. Fig. 7 shows the integrated current for MAST-U  $n = 2$  perturbations for various poloidal mode numbers  $m$  that are near the pedestal top. These are calculated as described in Appendix A. The values are given for the maximum RMP coil current possible in MAST-U ( $I_{\text{RMP}} = 8$  kAt). The maxima of the shielding current indicated by 'x' markers simultaneously indicate the optimal differential phase to achieve bifurcation of the respective mode. The optimal

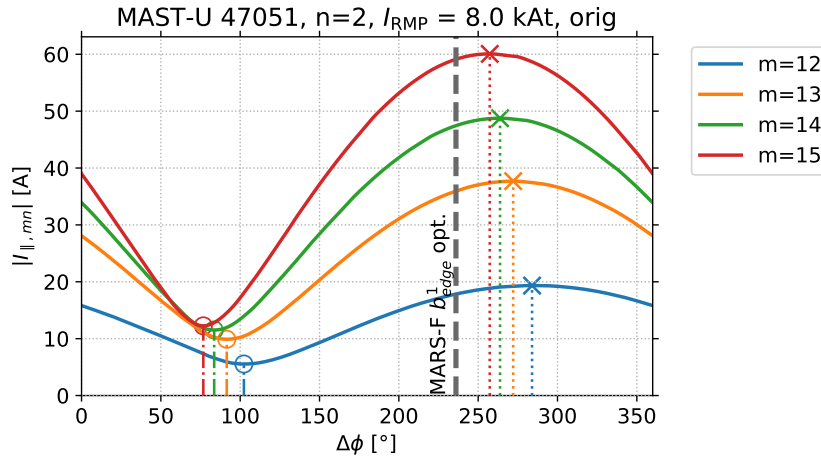


Figure 7: Integrated MARS-F current. The harmonics are given for Boozer angles. The maximum tends toward the optimum of the MARS-F metric  $b_{edge}^1$  (vertical dashed line) for higher mode numbers.

differential phase for the edge modes is, within a few degrees, in agreement with the prediction of the linear fluid metric  $b_{edge, res}^1$ , as shown in Fig. 3.

On the other hand, core modes, which should ideally not penetrate, have maxima and minima at higher differential phase values compared to the edge modes. As discussed above, for achieving ELM mitigation/suppression, it is desirable to minimize the core response, while maximizing the edge response. Hence, the optimal differential phase for the experiment lies within the minimum of the core modes and the maximum of the edge modes. This first assessment indicates the differential phase for optimal edge response, but it does not infer on actual mode penetration. For this, the kinetic metric with KilCA/QL-Balance is calculated (including the toroidal rescaling described in section 2.1.1). Figure 8 shows the kinetic metric for various poloidal mode numbers located near the pedestal top for  $n = 2$ . Indicated by dashed-dotted lines are the maxima of each mode. Notably, the magnitude of the metric does not imply the bifurcation of any of the modes.

In terms of optimal differential phase, the trend of  $D_{mn}$  goes toward the optimal value of  $b_{edge, res}^1$  for higher poloidal mode numbers. However, the cylindrical model of KilCA is not valid at the outermost edge of the plasma where the model's neoclassical reconstruction of the radial electric field loses validity. In fact, the kinetic criterion is mostly reliable (and hence it should be used) when considering the optimization around the pedestal top [14]. Whereas the fluid metrics are informing for regions closer to the separatrix, that is  $m = 22$  for  $q_{edge} = 11$  and  $n = 2$ . As a result, KilCA/QL-Balance computations provide a reliable pedestal-located optimization criterion which could be in principle a more effective predictor of RMP induced ELM control, than conventional fluid based metrics. Since a numerical comparison between the two metrics, in the same spatial region, is not possible yet, this may call for an experimental validation.

#### 4 Separatrix density scan

ELM control metrics are strongly influenced by the plasma response to the initial perturbation. In turn, the plasma response is primarily determined by the magnetic and

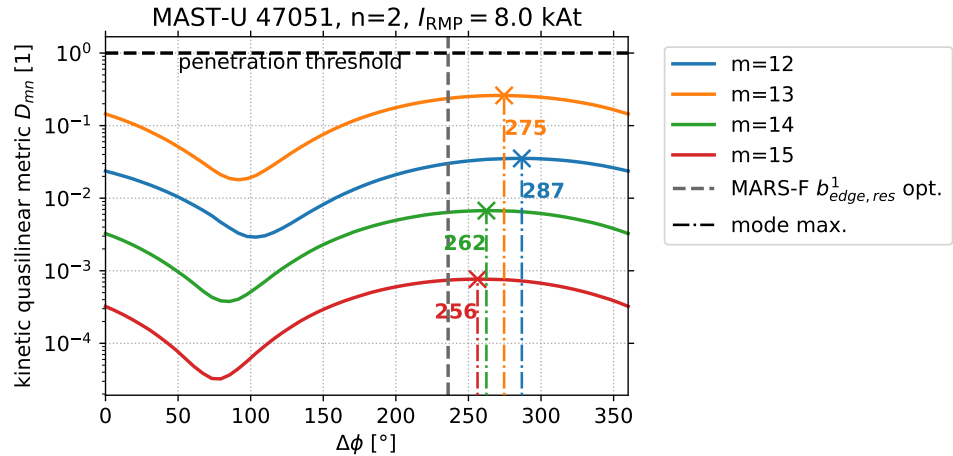


Figure 8: Kinetic quasi-linear metric for the  $n = 2$  perturbation. The maximum predicted by MARS-F is, again, highlighted by the vertical, dashed line.

kinetic characteristics of the equilibrium. To investigate and systematically characterize the effects of various kinetic features on ELM control metrics, it is advantageous to vary, one at a time, the kinetic properties of the initial equilibrium. In this work, motivated by the recent installation of a cryopump in the lower divertor of MAST-U, the dependence of the control metrics on the edge density profile has been examined. To maintain a conservative approach and isolate the effects of density alone, it has been assumed that the cryopump reduces the separatrix density while leaving the temperature profiles unaffected. To implement a separatrix density scan while keeping other aspects of the profile consistent, the density profile was truncated at approximately  $\sim 96\%$  of the normalized radius and then fitted using a modified hyperbolic tangent (*mtanh*) function. This method allows the density profile to be modeled with a small number of parameters, as detailed in [36]. While the separatrix density itself is not directly a degree of freedom of the fit, a systematic scan was achieved by fixing the pedestal height, width, and position, and increasing the pedestal gradient. In this way, the separatrix density scan effectively corresponds to a pedestal gradient scan. The results of this procedure are shown in Fig. 9. By increasing the pedestal gradient up to 10 times its original value, the separatrix density can be reduced by up to two orders of magnitude. To ensure a smooth connection between the modified edge profile and the original core profile, the core slope parameter was adjusted accordingly (see Fig 9 inset).

#### 4.1 Equilibrium reconstruction

By varying the density while keeping the temperature fixed, the pressure profile (and consequently the initial equilibrium) must change accordingly. Thus, the separatrix density scan inherently translates into an edge pressure scan. The resulting input pressure profiles are shown in Fig.10 (left panel). It is important to note that, due to the lack of additional constraints, the reconstructed pressure profile consists solely of the thermal contribution, expressed as  $P_{new} \propto n_e \cdot (T_e + T_i)$ . This differs significantly from the original pressure profile, which was constrained exclusively by the fit of magnetic measurements. A comparison between the magnetic EFIT++ pressure profile and the one implemented

for the first scan point (i.e., the case where the density profile matches the original one) is shown in the right panel of Fig. 10. In the thermal-only profile, a pronounced pedestal feature is evident in the edge region, which is absent in the magnetically constrained pressure profile. Additionally, the thermal-only profile exhibits a significantly higher integral  $\beta$  parameter. It is important to notice that the "kinetic" pressure used in the new scan is not magnetically constrained but corresponds to the equilibrium computed running CHEASE with the kinetic profiles fixing the EFIT++ boundary and current density profile. Realistically, the actual pressure profile likely lies between these two cases, which can be regarded as limiting scenarios. Despite the notable differences in pressure profiles, the computed equilibria show negligible variations in the  $q$ -profile (and thus in the plasma current), in fact, after recomputing the equilibrium, the  $q_{95}$  parameter changes are less than 2% with respect to the original one. Consequently, any observed differences in the plasma response can be attributed almost exclusively to the kinetic effects. For clarity sake, the equilibrium constrained by the magnetic measurements will be referred hereafter as 'magnetic equilibrium', whereas those obtained by reconstructing the pressure with the kinetic profiles will be called kinetic (or thermal) equilibria.

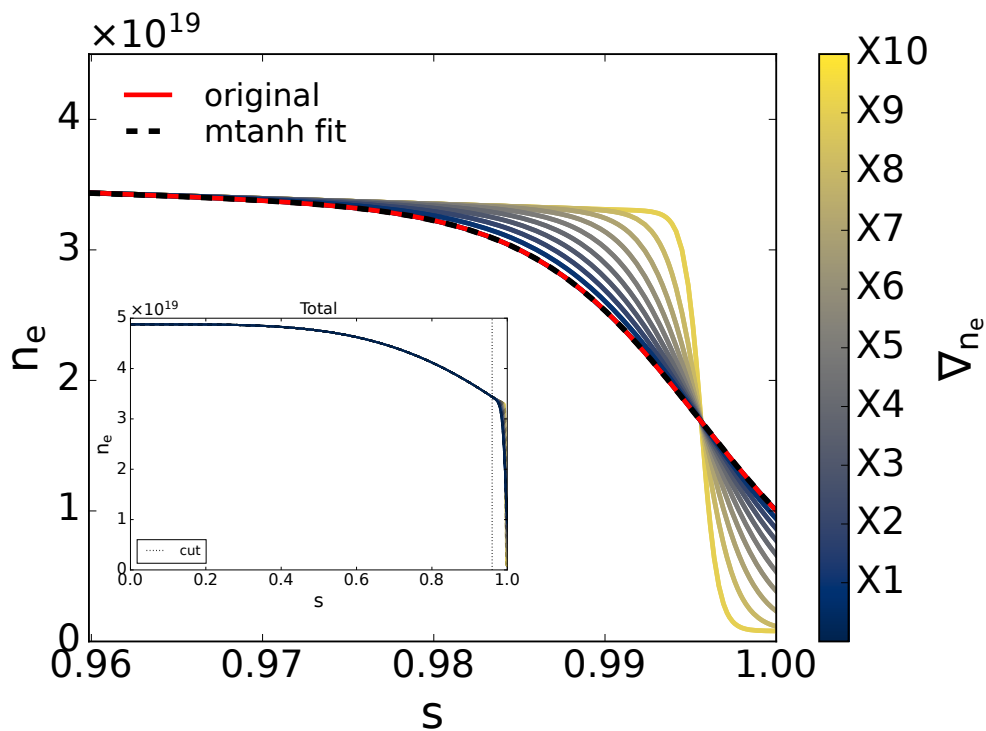


Figure 9: Full separatrix density scan. The original density profile, which corresponds to the 'X1' case of the scan, is cut at  $s = 0.96$  and fitted with an mtanh function. As the pedestal gradient increases (the curves turn yellow-ish) the separatrix density lowers. The inset, which reports the full profile for the whole scan, shows how the core region always coincide with the original one.

#### 4.2 Metrics evolution

For each point in the separatrix density scan, a plasma response run was performed using MARS-F, starting from the corresponding new equilibria and density profiles.

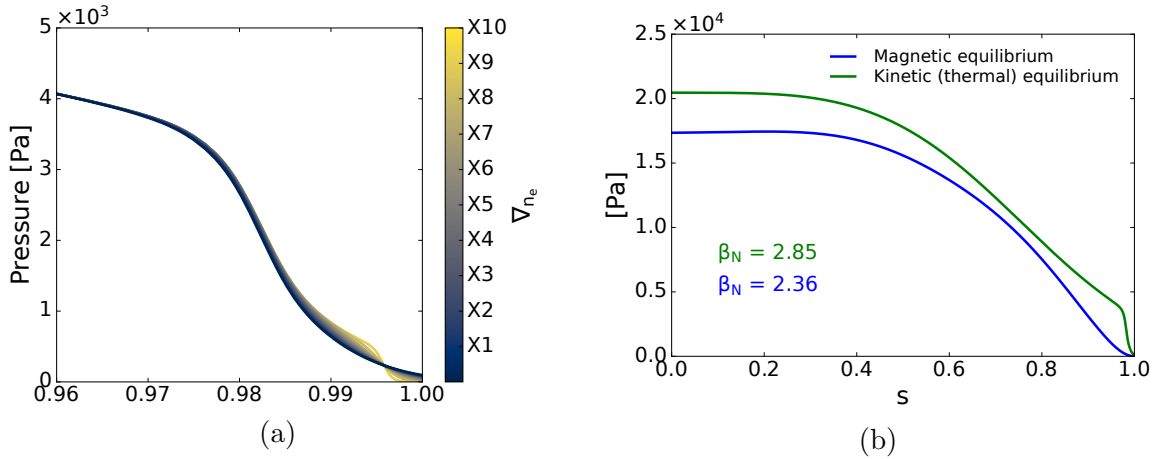


Figure 10: *a*: Pressure profiles scan obtained by increasing the density pedestal gradient and fixing the temperatures. *b*: Confront between magnetic constraint pressure profile (the original one), in blue, and the fixed-boundary, kinetically reconstructed profile, in green.

For simplicity, here the scan was conducted only for the  $n = 2$  case, which currently represents the best candidate configuration for the incoming ELM control experiments. In the next subsection, the evolution of the predicted optimal phases based on the different metrics, will be discussed as the pedestal gradient increases (i.e. as the separatrix density progressively lowers).

*Linear - resonant field metric* As can be observed in the left panel of Fig.11, when considering the most external pitch-aligned component of the perturbed radial field, a nearly monotonic decrease in the optimal phase is observed while  $\nabla n_e$  increases. The only exception is represented by the last scan point which suddenly jumps down of several degrees. Conversely, the magnitude of the edge-resonant field increases with the pedestal gradient, as indicated by the marker size. This trend suggests that steeper gradients and consequent lowering of the density close to the boundary may favour the perturbations penetration. The originally computed metrics, based on the initial equilibrium parameters, are indicated by the star symbols. Comparing the two cases, the phase that maximizes the vacuum field alignment shifts of  $\sim 10^\circ$ ; when adding the plasma response however, the optimum shifts of several degrees. Despite the evident evolution of the metric, the total variation of the optimal phase remains within  $\sim 40^\circ$ . By comparing this to Fig.3b, it becomes clear that the magnetic field remains close to its maximal value within this range. This demonstrates the robustness of the resonant field metric against variations in the density pedestal gradient.

*Linear - displacement ratio metric* The study of the evolution of the  $\xi_X/\xi_{mid}$  metric offers additional insights. As shown in Fig.11, right panel, where the ratio corresponding to the displacement at the upper X-point is depicted in red and at the lower X-point in green, an opposite behavior compared to the resonant field metric is observed. Up to the last one or two points of the scan, the trend exhibits a monotonic increase in the optimal phase for both curves. Interestingly, the magnitude of the displacement (represented by the marker size in the plot) also evolves differently depending on the X-point under

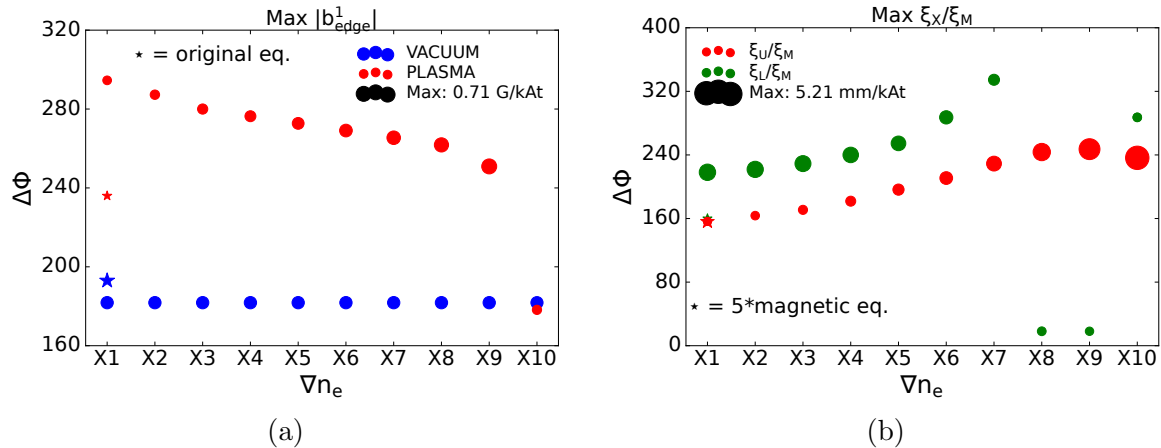


Figure 11: Fluid linear metrics scan. *a*: maximum of last resonant surface, pitch-aligned, radial perturbed field. *b*: maximum of the ratio between displacement at upper/lower X-points and mid-plane. In both figure the star marker identifies the values corresponding to the magnetically constrained equilibrium. The size of the dots scales with the magnitude of the perturbed field (left) and the displacement at the X-point (right) assuming 1kAt perturbation. The size of the stars scale similarly but in the case of the displacement ratio metrics it has been magnified by a factor 5 for visualization sake.

consideration. Specifically, the displacement at the upper X-point  $\xi_U$  increases with the pedestal gradient, whereas it decreases at the lower X-point  $\xi_L$ . This suggests that the region of the X-point where the induced perturbation acts depends significantly on the pedestal gradient' shape.

It should be noted that the anomalous values assumed by the last one or two points of the scan, already evidenced in the  $b_{res}^1$  metric analysis, could likely be associated to a possible unstable response of the plasma. In this eventuality, those values of the pedestal gradient would mark the threshold for the maximum pedestal steepness achievable.

Another notable difference between the red ( $\xi_{X_U}/\xi_{mid}$ ) and green ( $\xi_{X_L}/\xi_{mid}$ ) curves in the figure, is the range of optimal phase excursion during the scan. For the upper X-point displacement ratio, the phase variation remains within  $40^\circ$ , while the lower X-point displacement ratio spans about one-third of the toroidal angle. Moreover, as shown in Fig.3, in the right-lower quadrant, the peak around the optimal phase is narrower for this metric compared to the optimal region for  $b_{res}^1$ . This indicates that changes in the pedestal gradient could significantly influence the ELM control strategy based on this figure of merit. When comparing the metric computed using the magnetic equilibrium to the scanned cases, it is observed that its optimal phase aligns with only the first of the points of the  $\xi_{X_U}/\xi_{mid}$  curve. Conversely, the optimal phase for the  $\xi_{X_L}/\xi_{mid}$  ratio, which becomes the dominant contribution in the recomputed equilibria, shifts by approximately  $80^\circ$  and the displacement magnitude increases tenfold. This evidence, combined with the above considerations regarding the resonant field metric, suggest that the use of well-constrained input equilibria (both magnetically and kinetically) may have a critical impact when analyzing metrics which depend on the fine details of the plasma response.

*Quasi-linear - torque ratio metric* The ratio of torque generated at the edge to that in the core ( $\tau_{edge}/\tau_{core}$ ) proves to be the most robust metric against variations in separatrix

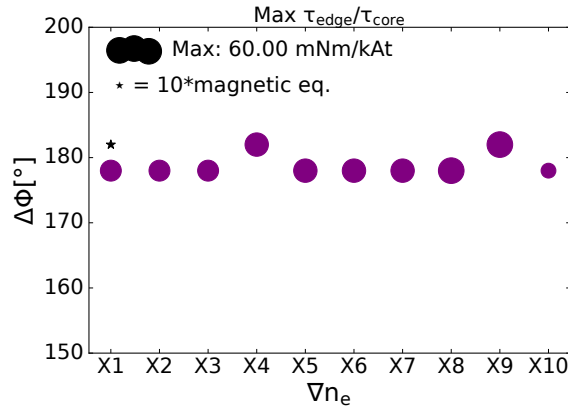


Figure 12: Fluid, quasi-linear metric scan. The size of the dots scales with the magnitude of total integrated torque injected assuming 1kAt perturbation. The star marker identifies the value corresponding to the magnetically constrained equilibrium. Its size has been magnified by a factor 10 for visualization sake

density as shown in Fig.12. However, notably the total torque injected (calculated as the sum of edge and core contributions) computed with kinetically constrains is approximately  $\sim 100\times$  larger than the one derived from the magnetic equilibrium. This can be visualized again in Fig.12 where the marker sizes now represent the total integrated torque magnitude. This increase may be primarily attributed to a significantly stronger braking induced in the edge region associated to an increase of the plasma response, which is in alignment with the conclusion drawn for the other linear metrics. These results further emphasize that while the  $\tau_{edge}/\tau_{core}$  optimum itself remains relatively invariant to the density scan, the absolute torque values are significantly influenced by adding kinetic constraints. Such large differences underscore, again, the necessity of incorporating accurate kinetic modeling when predicting or optimizing torque-driven effects in ELM control strategies.

*Quasi-linear - kinetic metric* Furthermore, the quasi-linear kinetic metric  $D_{mn}$  for the separatrix density scan cases is determined. To begin with, the difference in the constrained equilibria, as discussed in section 4.1, is again highlighted by the substantial difference in the magnitude of the response currents. The first kinetically constrained case, X1, clearly shows an integrated MARS-F current roughly three times as high as compared to the original magnetically constraint case for the mode  $m = 13$ . As a consequence, also the plasma response of KilCA is affected significantly.

Shown in Fig. 13a) is the quasi-linear kinetic metric at the differential phase of the maximum shielding current for each case. The jump from the magnetically constraint case (original) to the kinetically constraint cases is substantial and matches with the observations made in the previously discussed metrics. Most notably, now the metric predicts penetration for all the pedestal top modes even in the 'X1' case. This is a clear evidence of the correlation between penetration physics and the pressure profile structure. As the edge density gradient increases, the kinetic metric rises independently of equilibrium constraints. Since the density scan aims at emulating the effect of the cryopump, this suggests an advantageous effect of the pump on mode penetration for pedestal top modes, hence in principle favouring ELM control. Fig. 13b) shows the

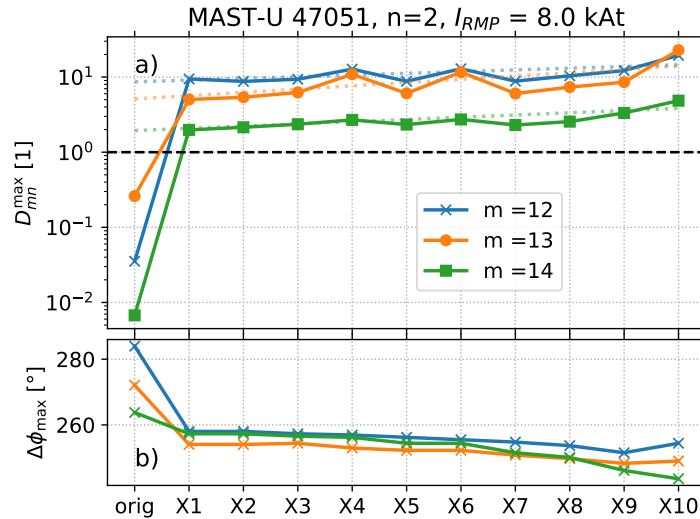


Figure 13: a) Kinetic metric for the maximum in the shielding current. b) Differential phase of the maximum shielding current.

differential phase of the maximum shielding current. The phase for the density scan cases shows an initial jump by approximately  $10^\circ$  to  $30^\circ$  from the original one. The trend of the differential phase is consistent with the behaviour of  $b_{res}^1$  as discussed above, even if the amount of change is reduced.

Summing up: during the scan, different metrics tend to behave differently. The  $b_{res}^1$  figure of merit ranges similarly to the  $\xi_{X_U}/\xi_M$  one, but with an opposite trend, whereas the  $\xi_{X_L}/\xi_M$  show a similar trend to the latter but different ranges of excursion in  $\Delta\Phi$ . In general, in all cases the last one or two points of the scan display a different behavior, this may be associated to a gradient too steep that may lead to some kind of unstable plasma response. Moreover, the  $\tau_{edge}/\tau_{core}$  metric is shown to be the most robust to the separatrix density scan with only the torque magnitude slightly varying with the pedestal gradient increase. The quasi-linear kinetic analysis shows a remarkable agreement with the  $b_{res}^1$  density scan trend. When including kinetic constraints in the equilibrium, the plasma response field grows non-negligibly. In particular, with the reconstructed equilibria the quasi-linear kinetic metric seems to be able to predict enough magnitude to finally achieve bifurcation (hence penetration). The observed change in this behavior may be attributed to an increase in the global beta, the introduction of a pedestal in the profile, or a combination of both. While an initial analysis indicates that the pedestal slope increases tenfold throughout the scan, the kinetic criterion also rises consistently but remains within the same order of magnitude. This suggests that the pedestal slope variation alone is unlikely to explain the abrupt transition from the magnetic to the kinetic equilibrium. Further work will be required to disentangle the individual contributions of these factors, possibly also including a fully non-linear analysis. Nevertheless, these observations strongly point out the importance of having a well constrained (both magnetically and kinetically) initial equilibrium when dealing with a plasma response analysis.

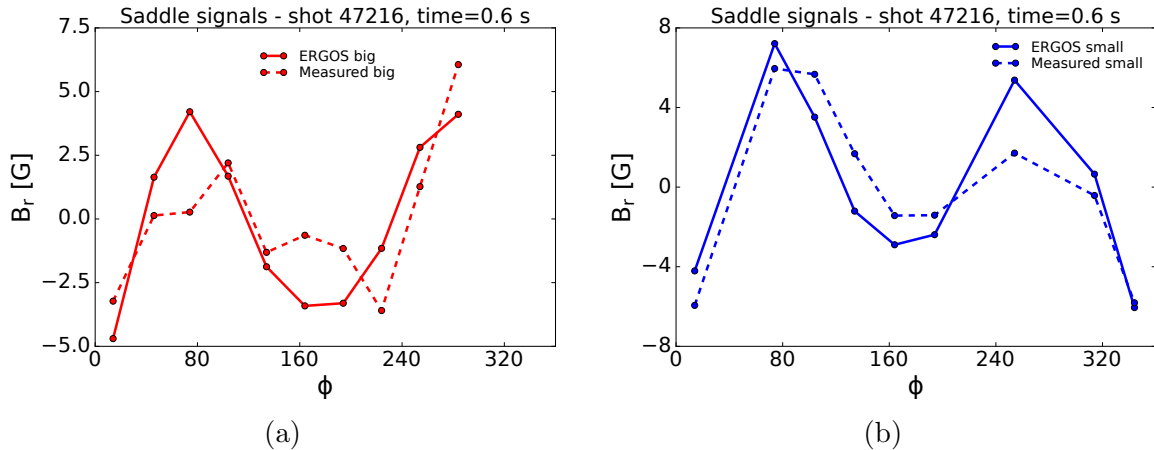


Figure 14: Comparison between the  $n > 0$  radial field predicted by the ERGOS model (solid lines) and as detected from the outboard saddle probes (dotted lines) during discharge #47216, at 600ms. Figure a) shows the *big* saddle signals whereas b) shows the *small* saddle signals. In both cases the ERGOS field has been obtained by averaging over the correspondent probe surface.

## 5 Error Field

Previous MAST-U campaigns faced significant challenges in achieving ELM control. Multiple attempts were conducted using the external coils in the  $n = 2$ ; however, none succeeded in reaching the threshold current necessary for ELM mitigation. Instead, in most cases, a locked mode (LM) was triggered, leading to early plasma termination [10]. A possible explanation for these failures lies in the presence of a non-negligible  $n = 2$  error field (EF), which could interfere with the externally induced perturbations. Historically, MAST-U has suffered from strong unwanted EFs originating from imperfections in the placement of poloidal field (PF) coils. The dominant EF contribution, in the  $n = 1$  configuration, has been successfully mitigated through mechanical adjustments, as confirmed by recent analyses [37]. However, no corrective measures have been implemented to address a potential  $n = 2$  component, as tilting or re-positioning the coils alone would not be effective. The failure of previous experiments has motivated a detailed investigation and characterization of the  $n = 2$  EF. The aim of this work is to quantify how the EF might modify the optimization of key metrics for ELM control. It should be noted that no attempt is made here to fully interpret experimental results, as non-linear physics should be accounted for once the perturbed fields successfully penetrates causing mode-locking. Instead, the focus lies on recomputing the optimal phases while incorporating a realistic, 3D EF model.

### *EF model*

The EF model was derived by integrating vacuum discharge measurements into the fully toroidal Biot-Savart code, ERGOS [38], within which the detailed geometry of the MAST-U PF coil system has been inserted [39]. As a first check, to provide procedure validation, the model computations were compared to the experimental measurements obtained from the #47216 vacuum discharge during which only one set of PF coils, namely P5 (upper and lower) was powered. The P5 coil set was chosen since, as can be seen later in the

discussion, its contribution to the Error Field turns out to be the predominant one. The measures were taken from the outboard saddles, a pair of toroidal arrays of saddle coils which, in MAST-U, allows to detect and evaluate the  $n > 0$  component of the radial field  $B_R$ . The pair is divided into the *big* and the *small* saddles, which are positioned at the same radial location (around  $R = 1.99\text{m}$  from the machine axis) with the center aligned with the machine's midplane. The coils have slightly different heights, hence the nomenclature, with the *big* spanning about 2 meters and the *small* around 1.6 meter. Being positioned right behind the P5, covering all their frames, these outboard saddles should detect the whole magnetic field produced by the poloidal coils, hence representing the best choice to compare vacuum discharges with the modeling results. It is worth noticing that the previous validation of the model was carried out in MAST which had worse capabilities in terms of radial field detection, instead, the comparison relied on measurements taken with three high-accuracy Hall probes that were installed ad-hoc [39].

Fig. 14 shows the comparison between the saddles measurements and the ERGOS results taken at the same radius and at the toroidal angles  $\phi$  corresponding to the probes location. To best match the observations, ERGOS computations are also averaged over the nominal coils area. It should be noted that neither the *big* nor the *small* saddles cover entirely the toroidal circumference, instead they provide total coverage only when superposed. To obtain the EF measurement, the equilibrium contribution (i.e the mean value) to the radial field must be taken out from the signal. Then, when comparing the remaining  $n > 0$  components with the correspondent ERGOS prediction, a satisfying match between model and measurements occurs. Notably, both the measured and the modelled signals display a clear  $n = 2$  behaviour.

A Fourier transform (FT) of the ERGOS 3D field was performed to correctly isolate the  $n = 2$  component. The computed vacuum field, for a unit current of 1kAt, is shown in the left panel of Fig. 15. According to equations 5, to compute the plasma response using MARS-F, the EF must be translated into an equivalent current on a conformal surface outside the plasma boundary. This is achieved using the Equivalent Surface Current (ESC) technique, which allows to prescribe an arbitrary magnetic field and to map it, by solving an inverse Biot-Savart problem, into the required input current [40]. This ensures that the plasma response calculation remains consistent within the entire domain enclosed by the ESC. The  $n = 2$  EF obtained via the ESC procedure was recomputed in MARS-F, and fig. 16 shows the excellent agreement between the vacuum field modeled by ERGOS and the results processed in MARS-F at the plasma boundary. The  $b_{res}^1$  poloidal spectra of the computed EF, for both vacuum-only and with plasma response runs, is reported in Fig. 17. For comparison, Fig. 18 shows the spectra (obtained with plasma response) for the upper and lower rows of RMPs coils. By observing the maximum values of each spectra, it can be immediately noted how the magnitude of the combined perturbation injected by the RMPs system, when in perfect constructive phase, would still of the same order of the intrinsic EF.

To identify the primary sources of the  $n = 2$  EF, computations were performed for each individual PF coil. Figure 19 indicates that the dominant contributions arise from the P4, P5, and P6 coil sets, with a minor contribution from the D coils. However,

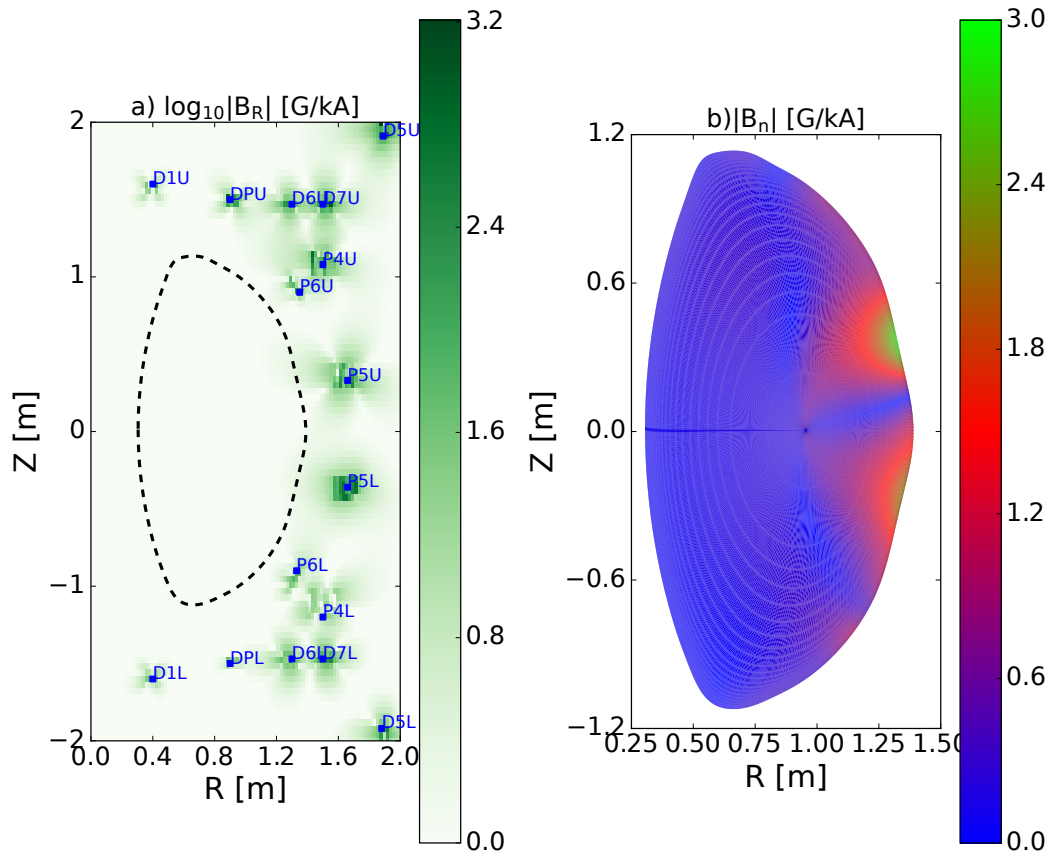


Figure 15: *a*:  $n = 2$  ERGOS  $B_R$  components (cylindrical coordinates) generated by the poloidal field coils (in blue) which distribution is marked in the poloidal section. The dashed line identifies the plasma boundary of #47051 at 611ms. *b*:  $n = 2$  normal component of the ERGOS field interpolated on the MARS-F grid. The ERGOS field has been computed singularly for each poloidal coil reported in the left figure, assuming  $1kAt$  feeding current.

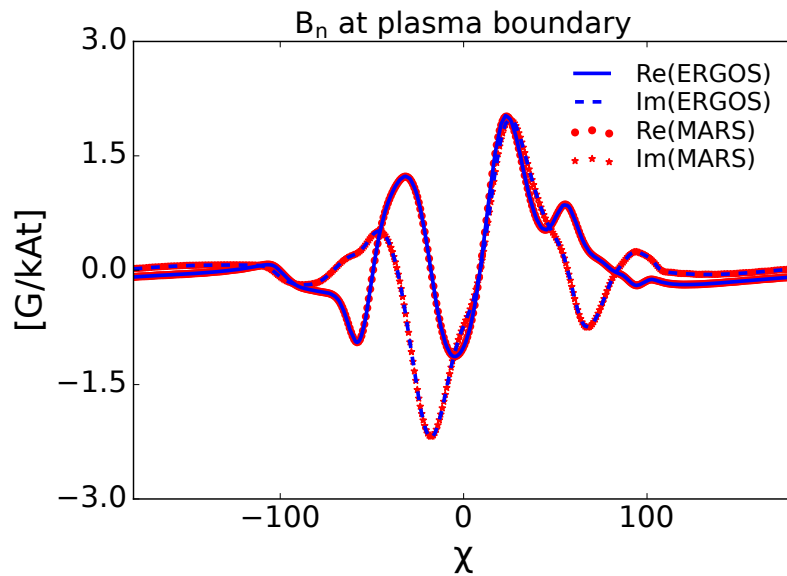


Figure 16: Poloidal distribution of the normal component of the  $n = 2$  vacuum error field at the plasma boundary, computed assuming  $1kAt$  current flowing in the poloidal field system. Solid lines represent  $Re(B_n)$ , whereas the dotted lines show  $Im(B_n)$ . Blue color identifies the ERGOS field, while the red color shows the same field but computed in MARS-F after applying the ESC technique.

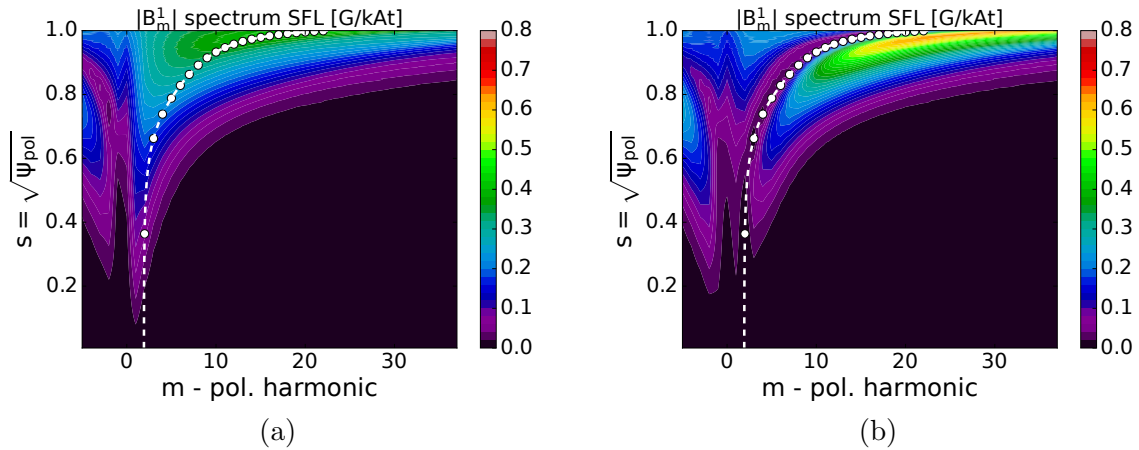


Figure 17: Poloidal spectrum of  $|b^1|$  per  $1kAt$  (in SFL coordinates) produced by the intrinsic  $n = 2$  EF. *a*: Vacuum field. *b*: Total field (vacuum + plasma response). The dotted white line corresponds to the  $q$  profile while the white dots identify the positions of rational surfaces.

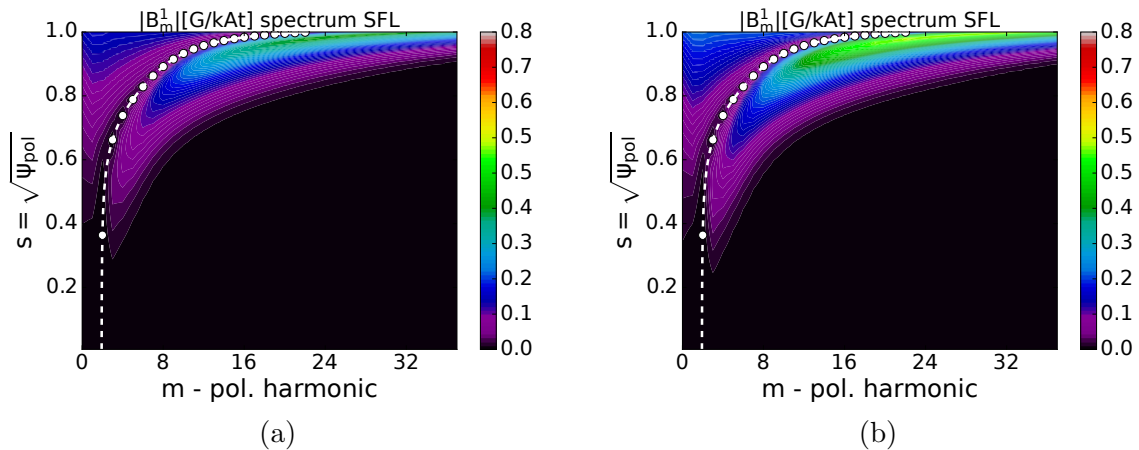


Figure 18: Poloidal spectrum of  $|b^1|$  (in SFL coordinates) total field produced by the the ELM coil sets in  $n = 2$  configuration, assuming an input current perturbation of  $1kAt$ . *a*: ELM coils, upper row. *b*: ELM coils, lower row. The dotted white line corresponds to the  $q$  profile while the white dots identify the positions of rational surfaces.

not all contributions are oriented in the same direction. The right panel of Fig. 19 illustrates the distribution of the perturbed radial field in the complex plane, showing partial cancellation between certain contributions like, for example, P4U and P6U, as well as P4L and P5L. The overall largest contribution comes from the P5 coils, with the upper P5U coil being dominant. This analysis suggests that distancing the plasma column from the P5 coil set could help reduce the intrinsic EF. Furthermore, as shown in Fig. 19 and Fig. 20, the green bar/marker in the complex plane represents the perturbation induced by the ELM coil system when in maximum constructive phase. A direct comparison with the EF components confirms that both effects produce perturbations of the same order of magnitude. This highlights the non-negligible impact of the intrinsic EF on the overall injected perturbation, potentially influencing the effectiveness of external RMP actuation.

To accurately assess the impact of EF-induced perturbations, the plasma response must account for the actual currents flowing in the PF coils during the experiment. In MAST-U, an external Rogowski coil is wrapped around each poloidal field coil, enabling the precise estimation of the currents that feed the PF system [41]. For discharge #47051

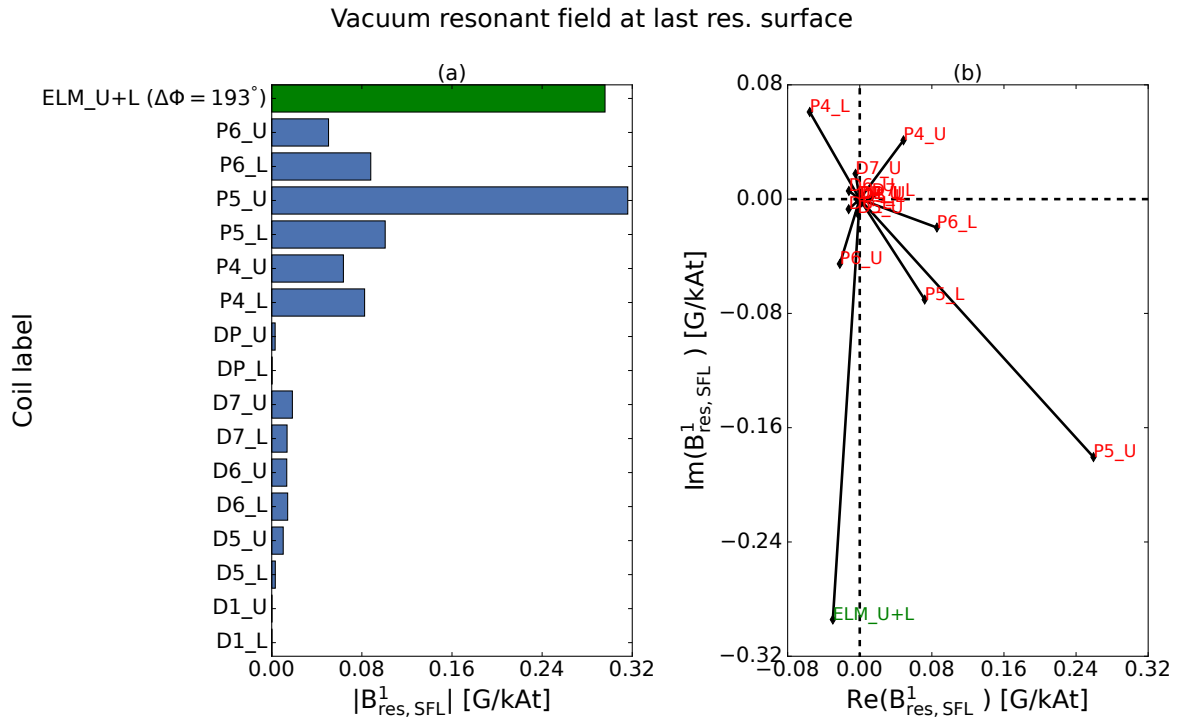


Figure 19:  $b^1$  resonant component (in SFL coordinate) of the vacuum  $n = 2$  EF and RMP perturbations computed at the  $q = 11$  rational surface. *a*: Histogram bars representing the absolute value of the field for each individual error field source. The green bar shows the absolute values correspondent to the sum of the ELM upper and lower row at the maximum alignment phase. *b*: representation of the field in the complex plane. Opposite vectors are in phase-opposition hence they would destructively add up. The  $b^1$  field is computed assuming  $1kAt$  current flowing in each coil.

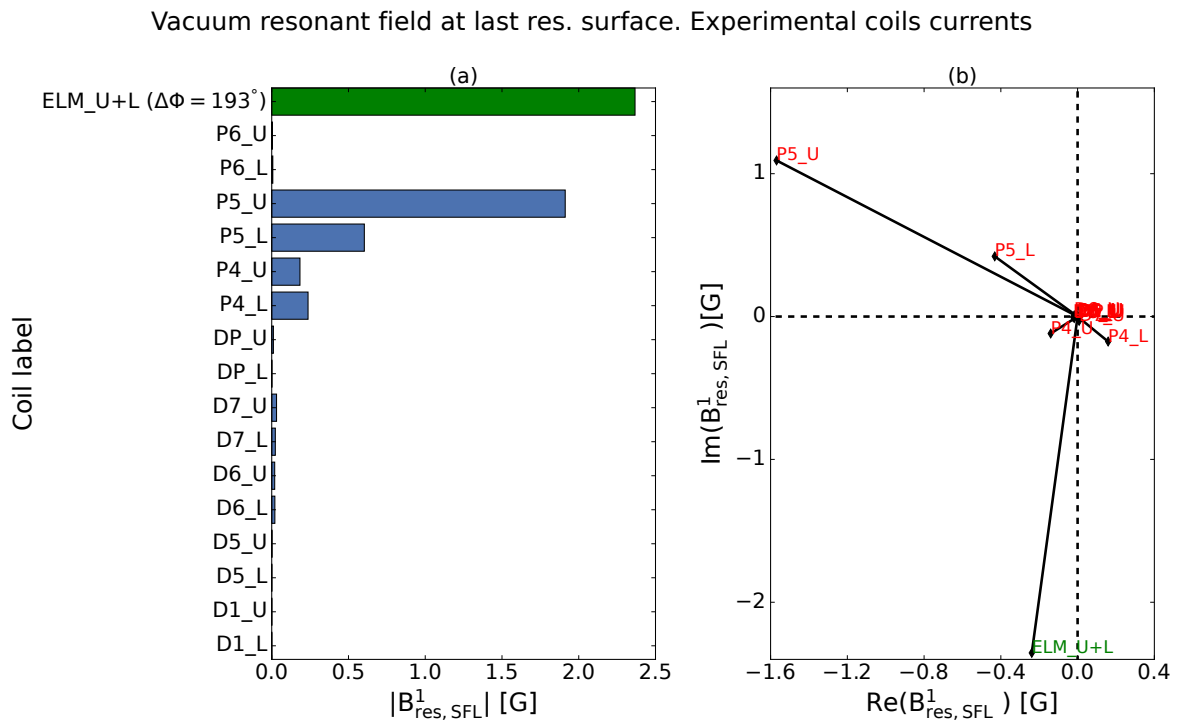


Figure 20: Same as Fig. 19 but here the  $b^1$  field is scaled with the experimental value of the source currents, taken at 611 ms for the discharge #47051, in each poloidal field coil. The RMP field is scaled with the maximum nominal current:  $8kAt$

	P4	<b>P5</b>	P6	D1	D5	D6	D7	DP
Upper	-2.89	<b>-6.05</b>	-0.08	3.91	-0.14	1.45	-1.71	-3.58
Lower	-2.87	<b>-5.99</b>	0.08	3.92	-0.13	1.44	-1.72	-3.61

Table 1: Values of the currents feeding each PF coil (both Upper and Lower) during shot #47051 at 611ms (in kAt), as measured by the external Rogowsky coil. P5 information are highlighted

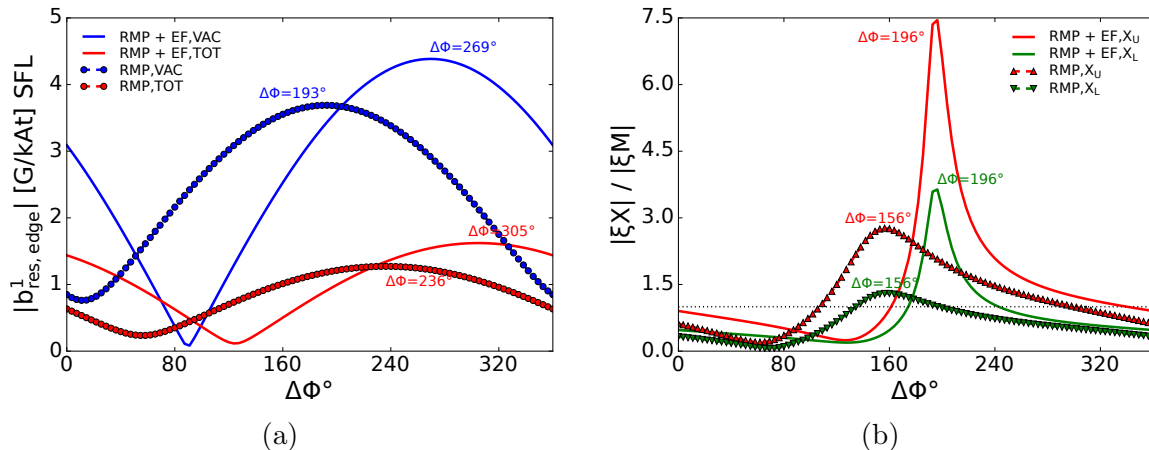


Figure 21:  $\Delta\Phi$  scan of the linear, fluid metrics adding the EF effect. *Left*:  $|b^1_{res}|$  metric. Here blue is the vacuum field while red is the total one. *Right*:  $\xi_L/\xi_M$  metric. The green curves corresponds to  $\xi_L$ , while the red one to  $\xi_U$ . The dotted lines correspond to the case without EF and with the RMP system at full power (8kAt). The solid lines are obtained by summing the EF

at 611 ms, these currents are reported in Table 1. Notably, the P5 coils, which already yield the strongest contribution, also appear to carry the largest fraction of the current. By re-scaling the ERGOS field with these experimentally measured currents, the actual effect of the EF plasma response during the discharge can be determined. Those re-scaled computations, shown in Fig. 20, confirm the P5 coils as the dominant sources of EF. Furthermore, the actual perturbation amplitude, due to the EF alone, reaches approximately  $\sim 3$ G, representing a substantial effect.

### EF correction to the metrics

By linearly combining the plasma response to the  $n = 2$  EF with the perturbation generated by the ELM control coils, the effect of the EF on key optimization metrics can be evaluated.

Fig. 21 shows the phase scan of both the linear metrics with the EF included compared to the curves obtained without. From the left panel, it is possible to appreciate the shift of the resonant field metrics. Both the vacuum and the total optimal alignments are moved ahead of  $\sim 70^\circ$ . The displacement ratio metric (right panel) displays a less drastic shift. The new optimum is found, for both the X-points, moved of about  $40^\circ$  with the ratio values strongly peaking above one for  $\xi_U$  for both  $\xi_L$ . However, at the original optimal phasing ( $\sim 156^\circ$ ), the ratios are now below unity. Hence, using this configuration would lead to a dominating kink-like response which would affect, potentially in a detrimental way, the core confinement. To investigate a little more in detail the influence of the EF, the evolution of the metric optimization is shown as the RMP current is ramped-up from 1 to 8kAt, which is the maximal nominal current of the

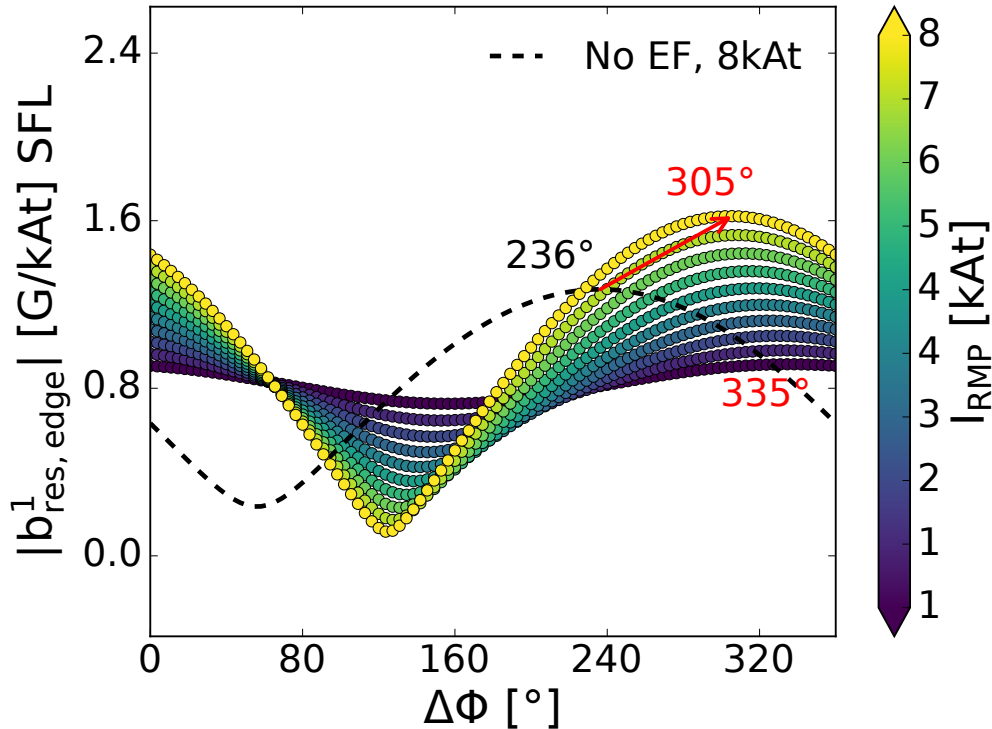


Figure 22: Total  $|b^1_{res,edge}|$  field metric for the case RMP+EF varying the RMP current from  $1kAt$  (blue-ish) to  $8kAt$  (yellow-ish), while fixing the latter. The black dashed curve shows the optimum trend for the total  $|b^1_{res,edge}|$  field, at  $8kAt$ , without the EF

coil set (Fig.22). Initially, the EF dominates the field response, shifting the optimization to  $\sim 335^\circ$ . However, as  $I_{RMP}$  increases, the intrinsic field is gradually compensated by the ELM coils which attempt to restore the original optimum. Indeed, once the current finally saturates, the predicted shift settles down at  $\sim 305^\circ$ . The optimal curve for the same metric but for the case without EF is also shown (black-dashed in the figure) for comparison sake. Aside from shifting the optimum, the inclusion of the EF also induces extra magnitude to the radial field which increases by approximately 20%.

When looking at the displacements metric, instead, the changes in the ratio values can be explained by observing Fig.23 which shows the  $\Delta\Phi$  dependence of the absolute value of  $\xi$  in each region considered. When adding the EF, all the displacements are shifted of few degrees. In particular, the displacement at the midplane (blue curve in Fig.23) becomes the most important one in the  $\Delta\Phi = [0 - 180]^\circ$  region, while the displacement at the upper X-point (red curve) would dominate in the rest of the parameter space. Most importantly, the maxima and the minima of each displacement curve get closer to alignment at similar relative phases. This suggests that the EF has a non-negligible influence on the plasma response and that it could in principle, when selecting the wrong choice of relative phasing, affect the core region.

The analysis of the torque ratio metric ( $\tau_{edge}/\tau_{core}$ ) further consolidate previous observations. Figure 24 shows that the optimal  $\Delta\Phi$ , when the EF is included, remains at the same phase of the original case. However the torque ratio value lowers getting closer to 1. With the introduction of the EF the edge and core torques become coupled

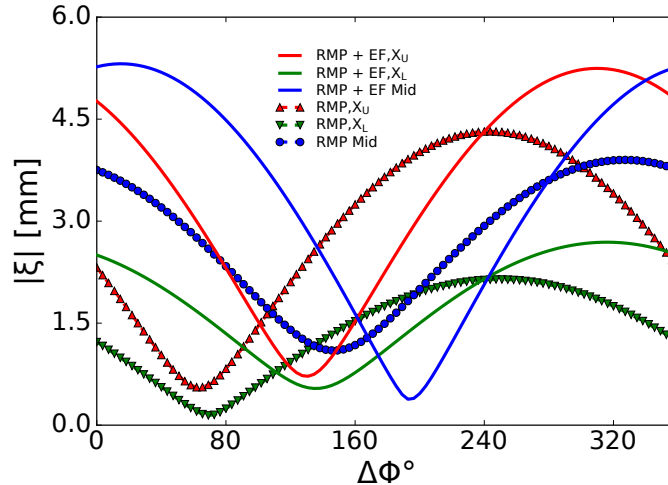


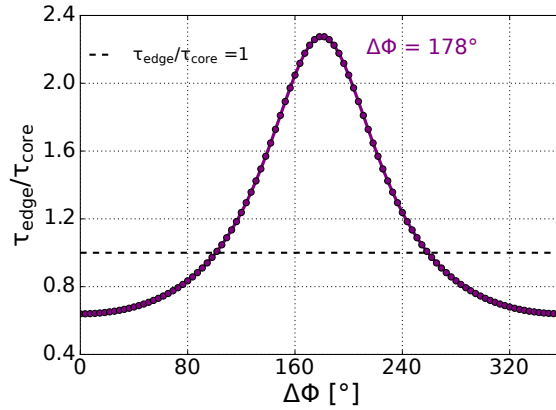
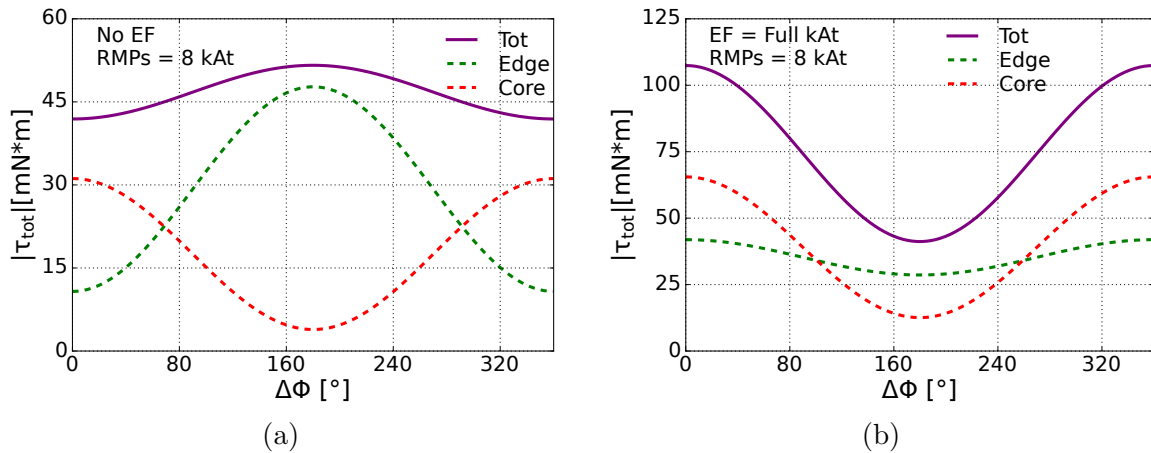
Figure 23: Magnitude of the displacements  $\xi$  measured at midplane (blue) and at both the X-points ( $\xi_U$ ,  $\xi_L$ ). The dotted lines correspond to the case without EF and RMPs at full power.

displaying minima and maxima aligned while, when considering the ELM control coils alone, the two regions were perfectly decoupled (see Fig25)a and b). Moreover, the core torque magnitude, being more dependent by the relative coil phase variation, also suggest the EF to be mostly affecting the core region of the plasma.

The core induced torque is also maximized at the RMPs optimal phase due to the presence of the EF. This could explain why previous experiments, in which RMPs were configured without accounting for the intrinsic field, ended with a lock-mode.

## 6 Conclusions

This study investigated the role of linear and quasi-linear modeling to understand, and eventually achieve, ELM control in the spherical tokamak MAST-U. Particular focus has been set on the correlation between the presence of an intrinsic Error Fields, the plasma response to external Resonant Magnetic Perturbations and the importance of having kinetic constraints on input equilibrium. With the recent installation of a cryopump in MAST-U lower divertor as a justification, a kinetic scan has been performed lowering the density value at the separatrix. Such a scan, when trying to maintain the maximum consistency with the original profiles, corresponds to steadily increase the pedestal density gradient. In the work the importance of having accurate equilibrium reconstructions has been highlighted, together with how the incorporation of both kinetic and magnetic constraints is crucial to precisely quantify the plasma response to the external perturbations, especially when resolving the pedestal region. In terms of optimization, this work evaluated the relative effectiveness of fluid and kinetic metrics in guiding ELM mitigation strategies. While, in general, validation with the experiments is essential to clarify which figure of merit should be applied, some considerations can be done about the reliability and the convenience for the use of each metric. The resonant radial field exhibits degrees of robustness under density pedestal gradient variations however the value of this metric relies only on predicting whether the system is able, or


 Figure 24:  $\tau_{edge}/\tau_{core}$  metric computed adding the effect of the EF.

 Figure 25: Integrated torque magnitudes, in absolute values, varying  $\Delta\Phi$ . Different spatial regions are denoted by colors with: **red** the core region, **green** the edge and **purple** the whole radius. *a*: torque injected by powering the RMP coils at full current (8kAt). *b*: torque injected by powering the RMP coils at full regime and including the EF scaled with the experimental currents.

not, to produce enough perturbation to achieve control. The results necessarily requires comparison with the experiment and it is usually device-dependent. It can, in turn, represent the fastest way to determine the optimal coil parameters when ELMs control has already been achieved on a device. In order to better understand the details of the response to the perturbation, the radial field metric should be complemented by a figure of merit that decouples the types of response, this could also be useful to prevent the onset of dangerous locked-modes while still investigating the coil-set parameter space. The displacement-based metric displays strong sensitivity to scenario changes, probably due to its extreme localization feature. While notable results have been previously achieved using this metric, it remains device-dependent and it may even turn out to be unreliable if the scenario characteristics happen to be too uncertain. Oppositely, the torque ratio metric, due to its global nature, is generically the most robust under different parameter variations such as toroidal mode number and kinetic profiles. Therefore, this metric could be utilized to assess the safety region of coil configurations prior to experimentation. Analysis of the composition of the fluid torque on MAST-U identifies the dominant role of the  $\mathbf{j} \times \mathbf{b}$  process which requires minimization in the core and maximization at the edge. So far only the optimal  $\Delta\Phi$  has been computed with the fluid quasi-linear torque which,

in principle, could also be used to derive the minimum current magnitude to achieve penetration by evolving the single-fluid momentum equation using the RMP torque as input source. This is currently left as future work.

The quasi-linear kinetic analysis, even if still unrefined, provided a remarkable comparison with the more traditional resonant field metric and an adequate agreement in the prediction of the optimal phase is demonstrated between the two workflows. The two metric both align in the suggestion that increasing the pedestal density gradient (i.e lowering the separatrix density) would favour the perturbation penetration. Moreover, a precise assessment of the RMPs magnitude needed to achieve the full penetration, even if time consuming, helps in determining the validity threshold for the linear metrics. This work has also shown how the penetration criterion is crucially dependent on the features of the pressure profile and therefore the importance of having a precisely constrained input equilibrium has been assessed. In future, comparing penetration dynamic as computed in the kinetic and fluid models would further deepen the physical understanding of RMPs applied to the ELM control. This pushes in the direction of directly benchmark the two quasi-linear frameworks. Moreover, careful analysis of the dependency on other kinetic parameters should be carried out to improve the characterization of the metric sensitivity to the pedestal parameters and enhance the modeling prediction capability.

In general, all these findings suggest that careful consideration of metric selection is essential to develop effective ELM control strategies in MAST-U.

Finally, this analysis characterized and quantified the dominant contribution to the  $n = 2$  component of the intrinsic EF associated with the PF system. The plasma response computations indicate that the EF may affect non-negligibly the core region, possibly compromising confinement and preventing ELM mitigation. Unfortunately, to mechanically correct the imperfections that produce all the unwanted  $n > 1$  components is not practically feasible, as it would require bending and deforming the coils shape, hence likely incurring in the risk of breaking them. Operation-wise, it could be a solution to try to adjust the plasma column to distance it from the P5 coil set. Alternatively, a possibility could be implementing error field correction with another set of external 3D coils such as the Error Field Correction coils (EFCc) which have been previously applied to correct the  $n = 1$  EF [11]. In the meanwhile, in this work alternative optimal phases have been computed including the model-based presence of the EF. Nevertheless, a thorough investigation should also include potential contributions from the toroidal field system and central solenoid to ensure a comprehensive evaluation of the intrinsic fields. This is, again, left as future work.

## Acknowledgments

We thanks Dr. N.Vianello and Dr. A.Stagni for helpful comments regarding the modeling of the pedestal profile. We also thanks Dr L.Piron and her student M.Gambrioli for the useful discussions about the Error Field presence in MAST-U. This work has been carried out within the framework of the EUROfusion Consortium, funded by the European Union via the Euratom Research and Training Programme (Grant Agreement No 101052200 — EUROfusion). Views and opinions expressed are however those of the author(s) only

and do not necessarily reflect those of the European Union or the European Commission. Neither the European Union nor the European Commission can be held responsible for them.

## Appendix A MARS-F shielding current integration

Bridging between MARS-F and the KilCA code requires the computation of the parallel component of the perturbed current density  $\mathbf{j}_{\parallel}$  which arise in response to any external magnetic perturbation. This can be done directly starting from MARS-F outputs. Indeed:

$$\mathbf{j}_{\parallel} = \frac{\mathbf{j} \cdot \mathbf{B}_0}{B_0} \quad (\text{A.1})$$

Where  $\mathbf{B}_0$  is the equilibrium field and  $B_0$  its modulus. This expression can be expanded in terms of MARS-F variables since  $B_0 = [B_0^1, B_0^2, B_0^3] = [0, \psi'/J, F/R^2]$  with  $\psi' = d\psi/ds$  and with  $\psi$  being the poloidal flux,  $J$  the metric Jacobian and  $F$  the poloidal current flux function and where 1,2,3 superscripts denominates the radial, poloidal and toroidal components respectively. Then:

$$j^i B_i = \frac{j^1 \psi' g_{12}}{J} + \frac{j^2 \psi' g_{22}}{J} + j^3 F \quad (\text{A.2})$$

$$B_0 = |\mathbf{B}_0| = \sqrt{B_0^i B_{i,0}} = \sqrt{0 + \psi' g_{22}/J^2 + (F/R)^2} \quad (\text{A.3})$$

With  $g_{ij}$  being the metric elements. Finally:

$$j_{\parallel}^{\text{MARS-F}} = \frac{j^1 \psi' g_{12}/J + j^2 \psi' g_{22}/J + j^3 F}{\sqrt{\psi' g_{22} + (F/R)^2}} \quad (\text{A.4})$$

The parallel current density determined in real space with MARS-F is expanded for Boozer coordinates in Fourier harmonics. For a single harmonic, we have

$$\mathbf{j}_{\parallel} = \mathbf{B}_0 \left( \frac{j_{\parallel}}{B_0} \right)_{\mathbf{m}} e^{i\vartheta_{B^m} + i\varphi_{B^n}}, \quad (\text{A.5})$$

where  $(j_{\parallel}/B_0)_{\mathbf{m}}$  is the Boozer harmonic of the current in toroidal geometry for the specific mode number  $\mathbf{m} = (m, n)$ . Note that the current calculated by MARS-F is given for a specific toroidal mode in geometrical angles. Hence, we need to account for a phase factor occurring in the transformation to the toroidal Boozer angle

$$j_{\parallel, n}(s_p, \vartheta_B) = j_{\parallel, n_g}^{\text{MARS-F}}(s_p, \vartheta_g(\vartheta_B)) e^{-inG(s_p, \vartheta_B)}, \quad (\text{A.6})$$

where  $n_g$  indicates the toroidal mode number for the geometrical angle used in MARS-F.

To get the mode specific parallel current, we integrate over a surface  $\mathbf{S}$ ,

$$I_{\parallel \mathbf{m}} = \int d\mathbf{S} \cdot \mathbf{B}_0 \left( \frac{j_{\parallel}}{B_0} \right)_{\mathbf{m}}. \quad (\text{A.7})$$

We choose the surface to be a toroidal surface, i.e. fixed toroidal angle, meaning that  $d\mathbf{S}_{\text{tor}} \cdot \mathbf{B}_0 = d\Psi_{\text{tor}}$ . Hence,

$$I_{\parallel \mathbf{m}} = \int d\Psi_{\text{tor}} \left( \frac{j_{\parallel}}{B_0} \right)_{\mathbf{m}}. \quad (\text{A.8})$$

To proceed we realize that, in the case of flux variables, the harmonic of the current density only depends on  $s = \sqrt{\Psi_{\text{pol}}^n}$ , where  $\Psi_{\text{pol}}^n$  is the normalized poloidal flux, or  $\Psi_{\text{pol}} = \Psi_{\text{pol}}^a s^2$  with the poloidal flux at the last closed flux surface,  $\Psi_{\text{pol}}^a$ . We further recall that the safety factor is defined as

$$q = \frac{d\Psi_{\text{tor}}}{d\Psi_{\text{pol}}}. \quad (\text{A.9})$$

With this, we can write  $d\Psi_{\text{tor}} = 2\Psi_{\text{pol}}^a s ds$ , with which the integration is written as

$$I_{\parallel\mathbf{m}} = 2\Psi_{\text{pol}}^a \int_{s_{\text{res}} - s_d}^{s_{\text{res}} + s_d} ds sq \left( \frac{j_{\parallel}}{B_0} \right)_{\mathbf{m}}. \quad (\text{A.10})$$

Note that the integration is over a region around the resonant surface with  $s_{\text{res}}$ . Previously [14], the width of this region was determined by a Gaussian fit, where  $s_d$  was taken to be five times the standard deviation. Here, however, it proved more consistent to integrate between the two neighbouring minima around a resonant surface.

## References

- [1] Hartmut Zohm. In: *Control. Fusion* 38 (1996), pp. 1213–1223.
- [2] A. Loarte et al. “ITER ELM Control Requirements, ELM Control Schemes and Required R and D”. In: *IAEA Fusion Energy Conference. Book of Abstracts* (2010). URL: [https://inis.iaea.org/search/search.aspx?orig\\_q=RN:43043504](https://inis.iaea.org/search/search.aspx?orig_q=RN:43043504).
- [3] P.T. Lang et al. “ELM pace making and mitigation by pellet injection in ASDEX Upgrade”. In: *Nuclear Fusion* 44.5 (2004), p. 665. DOI: [10.1088/0029-5515/44/5/010](https://doi.org/10.1088/0029-5515/44/5/010). URL: <https://dx.doi.org/10.1088/0029-5515/44/5/010>.
- [4] T.E. Evans et al. “Suppression of large edge localized modes in high confinement DIII-D plasmas with a stochastic magnetic boundary”. In: *Journal of Nuclear Materials* 337-339 (2005), pp. 691–696. ISSN: 0022-3115. DOI: <https://doi.org/10.1016/j.jnucmat.2004.10.062>.
- [5] A Kirk et al. “Effect of resonant magnetic perturbations with toroidal mode numbers of 4 and 6 on edge-localized modes in single null H-mode plasmas in MAST”. In: *Plasma Physics and Controlled Fusion* 55.1 (2012), p. 015006. DOI: [10.1088/0741-3335/55/1/015006](https://doi.org/10.1088/0741-3335/55/1/015006). URL: <https://dx.doi.org/10.1088/0741-3335/55/1/015006>.
- [6] A. Kirk et al. “Effect of resonant magnetic perturbations on low collisionality discharges in MAST and a comparison with ASDEX Upgrade”. In: *Nuclear Fusion* 55.4 (2015), p. 043011. DOI: [10.1088/0029-5515/55/4/043011](https://doi.org/10.1088/0029-5515/55/4/043011). URL: <https://dx.doi.org/10.1088/0029-5515/55/4/043011>.
- [7] T.E. Evans et al. “RMP ELM suppression in DIII-D plasmas with ITER similar shapes and collisionalities”. In: *Nuclear Fusion* 48.2 (2008), p. 024002. DOI: [10.1088/0029-5515/48/2/024002](https://doi.org/10.1088/0029-5515/48/2/024002). URL: <https://dx.doi.org/10.1088/0029-5515/48/2/024002>.

- [8] A Kirk et al. “Effect of resonant magnetic perturbations on ELMs in connected double null plasmas in MAST”. In: *Plasma Physics and Controlled Fusion* 55.4 (2013), p. 045007. DOI: [10.1088/0741-3335/55/4/045007](https://doi.org/10.1088/0741-3335/55/4/045007). URL: <https://dx.doi.org/10.1088/0741-3335/55/4/045007>.
- [9] A. Kirk et al. In: *Nuclear Fusion* 50 (3 2010). ISSN: 00295515. DOI: [10.1088/0029-5515/50/3/034008](https://doi.org/10.1088/0029-5515/50/3/034008).
- [10] D A Ryan et al. In: *Submitted to Plasma Physics and Controlled Fusion* (2024).
- [11] L. Piron et al. In: *Fusion Engineering and Design* (2020). DOI: [10.1016/j.fusengdes.2020.111932](https://doi.org/10.1016/j.fusengdes.2020.111932).
- [12] M W Shafer et al. In: *28th IAEA Fusion Energy Conference (FEC), London* (2020).
- [13] Yueqiang Liu, A. Kirk, and E. Nardon. “Full toroidal plasma response to externally applied nonaxisymmetric magnetic fields”. In: *Physics of Plasmas* 17 (12 2010). ISSN: 1070664X. DOI: [10.1063/1.3526677](https://doi.org/10.1063/1.3526677).
- [14] Markus Markl et al. “Kinetic study of the bifurcation of resonant magnetic perturbations for edge localized mode suppression in ASDEX Upgrade”. In: *Nuclear Fusion* 63 (12 2023). ISSN: 17414326. DOI: [10.1088/1741-4326/acf20c](https://doi.org/10.1088/1741-4326/acf20c).
- [15] H Ltitjens, A Bondeson, and O Sauter. In: *Computer Physics Communications* 97 (1996), pp. 219–260.
- [16] L.C. Appel and I. Lupelli. “Equilibrium reconstruction in an iron core tokamak using a deterministic magnetisation model”. In: *Computer Physics Communications* 223 (2018), pp. 1–17. ISSN: 0010-4655. DOI: <https://doi.org/10.1016/j.cpc.2017.09.016>.
- [17] MAST Upgrade team et al. “First MAST-U Equilibrium Reconstructions using the EFIT++ code”. In: *48th EPS Conference on Plasma Physics 27 June - 1 July 2022*. Europhysics conference abstracts. European Physical Society (EPS), 2022. URL: <https://www.epsplasma2022.eu/>.
- [18] D. A. Ryan et al. “Numerically derived parametrisation of optimal RMP coil phase as a guide to experiments on ASDEX Upgrade”. In: *Plasma Physics and Controlled Fusion* 59 (2 2017). ISSN: 13616587. DOI: [10.1088/1361-6587/59/2/024005](https://doi.org/10.1088/1361-6587/59/2/024005).
- [19] A Bondeson and R Iacono. “Ideal stability of cylindrical plasma in the presence of mass flow”. In: (1988).
- [20] A Bondeson, Yueqiang Liu, and C M Fransson. “Active control of resistive wall modes in the large-aspect-ratio tokamak Related content Active feedback stabilization of high beta modes in advanced tokamaks”. In: *Nuclear Fusion* (2002).
- [21] R. Fitzpatrick. “Nonlinear error-field penetration in low density ohmically heated tokamak plasmas”. In: *Plasma Physics and Controlled Fusion* 54 (9 2012). ISSN: 07413335. DOI: [10.1088/0741-3335/54/9/094002](https://doi.org/10.1088/0741-3335/54/9/094002).
- [22] I. B. Ivanov et al. “Kinetic Linear Model of the Interaction of Helical Magnetic Perturbations with Cylindrical Plasmas”. In: *Physics of Plasmas* 18.2 (2011), p. 022501.

- [23] A F Martitsch et al. “Effect of 3D magnetic perturbations on the plasma rotation in ASDEX Upgrade”. In: *Plasma Physics and Controlled Fusion* 58.7 (2016), p. 074007. DOI: [10.1088/0741-3335/58/7/074007](https://doi.org/10.1088/0741-3335/58/7/074007).
- [24] J-K Park, A.H. Boozer, and A.H. Glasser. “Computation of Three-Dimensional Tokamak and Spherical Torus Equilibria”. In: *Physics of Plasmas* 14 (2007), p. 052110.
- [25] Jong-Kyu Park, Allen H Boozer, and Jonathan E Menard. “Shielding of External Magnetic Perturbations by Torque in Rotating Tokamak Plasmas”. In: *Physics of Plasmas* 16 (2009), p. 082512.
- [26] J.-K. Park and N. C. Logan. “Self-Consistent Perturbed Equilibrium with Neoclassical Toroidal Torque in Tokamaks”. In: *Physics of Plasmas* 24.3 (2017), p. 032505.
- [27] Jong Kyu Park et al. “Importance of plasma response to nonaxisymmetric perturbations in tokamaks”. In: *Physics of Plasmas* 16 (5 2009). ISSN: 1070664X. DOI: [10.1063/1.3122862](https://doi.org/10.1063/1.3122862).
- [28] “3D field phase-space control in tokamak plasmas”. In: *Nature Physics* 14 (12 2018), pp. 1223–1228. ISSN: 17452481. DOI: [10.1038/s41567-018-0268-8](https://doi.org/10.1038/s41567-018-0268-8).
- [29] Yueqiang Liu et al. “ELM control with RMP: Plasma response models and the role of edge peeling response”. In: *Plasma Physics and Controlled Fusion* 58 (11 2016). ISSN: 13616587. DOI: [10.1088/0741-3335/58/11/114005](https://doi.org/10.1088/0741-3335/58/11/114005).
- [30] K. C. Shaing, S. A. Sabbagh, and M. S. Chu. “An approximate analytic expression for neoclassical toroidal plasma viscosity in tokamaks”. In: *Nuclear Fusion* 50 (2 2010). ISSN: 00295515. DOI: [10.1088/0029-5515/50/2/025022](https://doi.org/10.1088/0029-5515/50/2/025022).
- [31] Y. Sun et al. “Modelling of the neoclassical toroidal plasma viscosity torque in tokamaks”. In: *Nuclear Fusion* 51 (5 2011). ISSN: 00295515. DOI: [10.1088/0029-5515/51/5/053015](https://doi.org/10.1088/0029-5515/51/5/053015).
- [32] Zhirui Wang et al. “Theory comparison and numerical benchmarking on neoclassical toroidal viscosity torque”. In: *Physics of Plasmas* 21 (4 2014). ISSN: 1070664X. DOI: [10.1063/1.4869251](https://doi.org/10.1063/1.4869251).
- [33] Xu Yang et al. “Toroidal modeling of the  $n = 1$  intrinsic error field correction experiments in EAST”. In: *Plasma Physics and Controlled Fusion* 60 (5 2018). ISSN: 13616587. DOI: [10.1088/1361-6587/aab30f](https://doi.org/10.1088/1361-6587/aab30f).
- [34] L. Li et al. “ELM control optimization for various ITER scenarios based on linear and quasi-linear figures of merit”. In: *Physics of Plasmas* 27 (4 2020). ISSN: 10897674. DOI: [10.1063/1.5139890](https://doi.org/10.1063/1.5139890).
- [35] R. Nazikian et al. “Pedestal Bifurcation and Resonant Field Penetration at the Threshold of Edge-Localized Mode Suppression in the DIII-D Tokamak”. In: *Phys. Rev. Lett.* 114.10 (2015), p. 105002. DOI: [10.1103/PhysRevLett.114.105002](https://doi.org/10.1103/PhysRevLett.114.105002).
- [36] L. Frassinetti et al. “Pedestal structure, stability and scalings in JET-ILW: The EUROfusion JET-ILW pedestal database”. In: *Nuclear Fusion* 61 (1 2021). ISSN: 17414326. DOI: [10.1088/1741-4326/abb79e](https://doi.org/10.1088/1741-4326/abb79e).

- [37] M. Gambrioli et al. “Investigation of intrinsic error fields in MAST-U device”. In: *Fusion Engineering and Design* 205 (2024), p. 114544. ISSN: 0920-3796. DOI: <https://doi.org/10.1016/j.fusengdes.2024.114544>.
- [38] M. Bécoulet et al. “Numerical study of the resonant magnetic perturbations for Type I edge localized modes control in ITER”. In: *Nuclear Fusion* 48.2 (2008), p. 024003. DOI: [10.1088/0029-5515/48/2/024003](https://doi.org/10.1088/0029-5515/48/2/024003).
- [39] A. Kirk et al. “Measurement, correction and implications of the intrinsic error fields on MAST”. In: *Plasma Physics and Controlled Fusion* 56 (10 2014). ISSN: 13616587. DOI: [10.1088/0741-3335/56/10/104003](https://doi.org/10.1088/0741-3335/56/10/104003).
- [40] “Modelling intrinsic error field correction experiments in MAST”. In: *Plasma Physics and Controlled Fusion* 56 (10 2014). ISSN: 13616587. DOI: [10.1088/0741-3335/56/10/104002](https://doi.org/10.1088/0741-3335/56/10/104002).
- [41] D. A. Ryan et al. “Initial progress of the magnetic diagnostics of the MAST-U tokamak”. In: *Review of Scientific Instruments* 94 (7 2023). ISSN: 10897623. DOI: [10.1063/5.0156334](https://doi.org/10.1063/5.0156334).